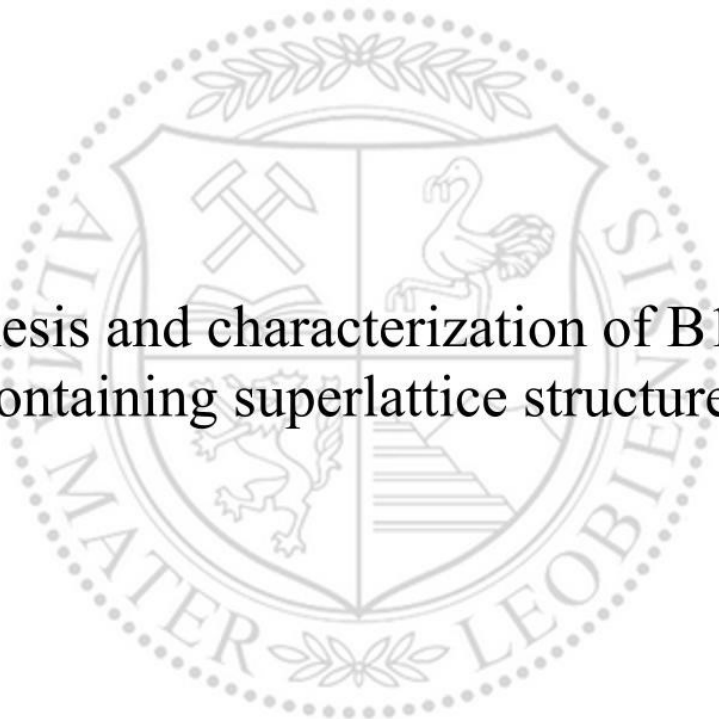




Chair of Functional Materials and Materials Systems

Master's Thesis



Synthesis and characterization of B1-AlN  
containing superlattice structures

Maria-Theresia Becker, BSc

October 2022

This research was funded by the Austrian Science Fund (FWF) [I 4720 "Designing toughening concepts for future hard coatings"].



**MONTANUNIVERSITÄT LEOBEN**  
www.unileoben.ac.at

**EIDESSTATTLICHE ERKLÄRUNG**

Ich erkläre an Eides statt, dass ich diese Arbeit selbständig verfasst, andere als die angegebenen Quellen und Hilfsmittel nicht benutzt, und mich auch sonst keiner unerlaubten Hilfsmittel bedient habe.

Ich erkläre, dass ich die Richtlinien des Senats der Montanuniversität Leoben zu "Gute wissenschaftliche Praxis" gelesen, verstanden und befolgt habe.

Weiters erkläre ich, dass die elektronische und gedruckte Version der eingereichten wissenschaftlichen Abschlussarbeit formal und inhaltlich identisch sind.

Datum 14.10.2022

*Maria-Theresia Becker*

Unterschrift Verfasser/in  
Maria-Theresia Becker

## **Acknowledgements**

First, I want to thank Prof. Dr. Christian Mitterer for giving me the opportunity of writing this master's thesis at the chair of functional materials and material systems and for his input during the correction of this thesis.

Special thanks go to Dr. Matthias Bartosik, within whose project this thesis was created. I am very thankful for his motivated, experienced, and time-consuming mentoring throughout the entire master's thesis.

I would also like to thank Mag. Velislava Terziyska and Karl-Heinz Pichler for their support during the experiments for this thesis.

Furthermore, I would like to thank Dr. Michal Zitek for his help and patience whenever I needed help with the deposition system "Debbie".

I would also like to acknowledge all members of the Thin-film group for helping me in any case.

Finally, I am very grateful to my family and friends, who were always supportive and encouraged me in difficult moments. Especially, I want to thank my parents, who have made my studies in Leoben possible.

## Abstract

Due to their excellent mechanical properties, nitride superlattices (SLs) are used industrially as hard protective coatings, e.g., to protect and enhance the performance of cutting tools in the machining industry. This master's thesis deals with the synthesis and characterization of chromium nitride (CrN) / aluminum nitride (AlN) SL coatings with AlN stabilized in its metastable B1 structure. The films were synthesized in an unbalanced reactive magnetron sputtering system equipped with computer-controlled mechanical shutters. Polycrystalline SLs were obtained by using Si (100) as substrate material, while single-crystal SLs develop when depositing on MgO (100). The films' structural and mechanical properties were determined by X-ray diffraction and nanoindentation, respectively. Polycrystalline SLs with 4 nm CrN / 2 nm AlN architecture had a hardness of  $28.2 \pm 0.7$  GPa, while an even higher hardness of  $33.3 \pm 1.3$  GPa was measured for single-crystal SLs with the same architecture. The SLs were about 6.5 GPa harder than monolithic CrN on the same type of substrate. The hardness of B3-AlN containing 4 nm CrN / 5 nm AlN SL films was with  $24.8 \pm 1.0$  and  $27.8 \pm 1.0$  GPa for films on Si (100) and MgO (100), respectively, lower compared to the exclusively B1-structured SLs. Explanations for the SL hardness effect and the influence of interfaces between the nanolayers and columnar grain boundaries on the mechanical behavior of SLs are discussed.

## Kurzfassung

Aufgrund ihrer herausragenden mechanischen Eigenschaften werden Nitrid-Superlattice-Beschichtungen (SL) industriell genutzt. Beispielsweise werden sie in der Zerspanungsindustrie als Schutz und zur Verbesserung der Performance von Schneidwerkzeugen aufgebracht. Diese Masterarbeit beschäftigt sich mit der Herstellung und Charakterisierung von Chromnitrid (CrN) / Aluminiumnitrid (AlN) SL-Schichten, in denen AlN in seiner metastabilen B1-Struktur stabilisiert wurde. Die Herstellung erfolgte mittels Magnetronspütern in einer Beschichtungsanlage, welche mit computergesteuerten, mechanischen Shuttern ausgestattet ist. Durch die Verwendung verschiedener Substrate wurden polykristalline SLs (Si (100) Substrate) und einkristalline SLs (MgO (100) Substrate) hergestellt. Die Struktureigenschaften wurden mittels Röntgendiffraktometrie und die mechanischen Eigenschaften mittels Nanoindentation ermittelt. Die gemessene Härte von SLs mit einer 4 nm CrN / 2 nm AlN Architektur beträgt  $28.2 \pm 0.7$  GPa auf Si (100) -Substraten und  $33.3 \pm 1.3$  GPa auf MgO (100) -Substraten. Damit konnte auf beiden Substraten eine Härtesteigerung von 6.5 GPa gegenüber der zugehörigen monolithischen Chromnitrid-Schicht erreicht werden. Auf 4 nm CrN / 5 nm AlN SLs, welche B3-AlN enthalten, liegt die gemessene Härte mit  $24.8 \pm 1.0$  und  $27.8 \pm 1.0$  GPa auf Si (100) und MgO (100) Substraten unter der Härte jener Schichten, in welchen AlN vollständig in seiner B1-Struktur stabilisiert wurde. Eine Diskussion über die Härtesteigerung in SLs, sowie über den Einfluss von Grenzflächen zwischen den Layer-Materialien und von säulenförmigen Korngrenzen auf die mechanischen Eigenschaften runden diese Masterarbeit ab.

## Content

1.	Introduction.....	8
2.	Theoretical background .....	9
2.1.	Material system .....	9
2.1.1.	SL films.....	9
2.1.2.	CrN and AlN .....	9
2.1.3.	CrN/AlN SL coatings.....	12
2.2.	Deposition of SL films via reactive magnetron sputtering .....	13
2.2.1.	Sputter deposition.....	13
2.2.2.	Reactive sputtering .....	15
2.2.3.	Film formation and structure zone model .....	15
2.3.	Mechanical properties of SL films .....	17
3.	Experimental details.....	19
3.1.	Film fabrication.....	19
3.1.1.	Deposition setup .....	19
3.1.2.	Substrate preparation .....	19
3.1.3.	Film deposition .....	20
3.2.	Structure analysis .....	21
3.3.	Film thickness measurement.....	22
3.4.	Measurement of hardness and Young's modulus.....	22
4.	Results and discussion.....	23
4.1.	Film deposition .....	23
4.1.1.	Deposition parameter study .....	23
4.1.2.	Final parameter choice.....	25

4.1.3.	Critical layer thickness of monolithic CrN .....	26
4.1.4.	Deposition of SL films .....	29
4.2.	Film characterization .....	30
4.2.1.	Film structure .....	30
4.2.2.	Film thickness and bilayer period.....	37
4.2.3.	Hardness and Young's modulus .....	37
5.	Summary .....	44
6.	References.....	46

## 1. Introduction

Hard coatings are widely used in industry to protect tools, dies and molds from severe loads and harsh environments [1,2]. For example, these coatings improve the performance and lifetime of cutting tools, which are exposed to elevated temperatures, friction, wear, corrosion, oxidation, and fatigue. Dependent on the application, typically nitrides, carbides, carbonitrides, borides, boronitrides or oxides are used [3]. The properties of hard coating materials have essentially been continuously improved in three ways over the past decades: by optimizing the film growth process (parameters), by adding alloying elements and/or via the coating architecture or nanostructure (multilayer, nanolayer, nanocomposite) [3,4].

Superlattice (SL) coatings are artificially layered thin films, in which two or more materials with a thickness of only a few nanometers are epitaxially grown on top of one another [5,6]. Compared with their monolithic counterparts, SLs exhibit better mechanical properties and thermal stability [6]. Due to their excellent properties, SL coatings have evoked much scientific attention and are used industrially as wear-protective coatings [7]. Another aspect of SLs is that metastable materials with interesting properties can be synthesized, which do not exist as bulk materials under ambient conditions [8].

The aim of this thesis was to synthesize and characterize SL films with metastable B1-aluminum nitride (AlN) stabilized in chromium nitride/aluminum nitride (CrN/AlN) SL films. Also, multilayer films without a complete stabilization of B1-AlN and monolithic films were produced for comparison. While this master thesis focusses on the synthesis and the determination of the basic properties of the films such as their structure, hardness, and Young's modulus, a further motivation behind the fabrication of the films was to determine the films' fracture toughness in a follow up study to this thesis. Due to the volume increase accompanying the phase transformation from metastable cubic B1-AlN to thermodynamically stable hexagonal B3-AlN, AlN has the potential for phase transformation toughening [9–11].



## 2. Theoretical background

This chapter gives a short theoretical overview of the chosen material system, the applied film deposition method, and the mechanical film properties.

### 2.1. Material system

#### 2.1.1. SL films

SL coatings are periodically layered thin films, where two or more materials with a thickness of a few nanometers are epitaxially grown on top of one another (Figure 1) [5,6]. SL structures can be single crystalline or polycrystalline. Structural features are the crystal structure, the epitaxial relationship of layers, preferred orientations and strains and defects at the interface. Chemically, the bilayer period, the composition of inlayers and interfaces and the interface width are describing a SL film. Coherency strains are a main feature of SL films. As lattice constants are likely to be not equal, both materials are strained to obtain a coherent interface. With increasing layer thickness, mismatch strains can be accommodated by misfit dislocations [5].

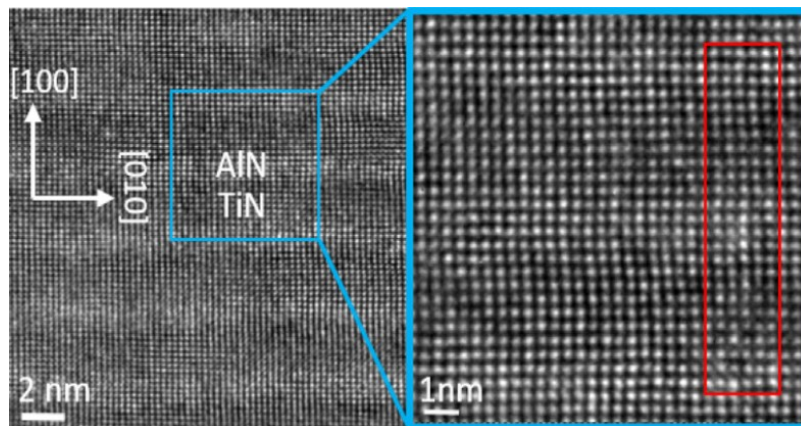


Figure 1: high resolution transmission electron microscopy (HRTEM) image of a SL film [57].

#### 2.1.2. CrN and AlN

A classification of nitrides can be done by their bonding character [12]:

- Ionic nitrides: are nitrides of alkali and alkaline-earth metals.
- Covalent nitrides: are non-conductors or semi-conductors. Important representatives are BN, AlN, GaN and SiN.

- Interstitial nitrides: have a primarily metallic bonding character. They are also known as transition metal nitrides. Examples are TiN, ZrN and CrN.

**CrN**

CrN is assignable to the group of transition metal nitrides. This group has a metallic bonding character. Electrical and thermal conductivities are high, and they also exhibit a metallic appearance. But, in comparison with metals, they are very hard and brittle [12]. As they are hard, wear-resistant, corrosion-resistant, thermally stable, and oxidation-resistant, transition metal nitrides are frequently used as coatings on metal cutting tools [12,13].

As shown in Figure 2, two different nitrides can be found in the Cr-N equilibrium binary phase diagram. The brittle Cr<sub>2</sub>N occurs at lower nitrogen contents. At higher nitrogen contents, the cubic CrN forms [14]. The aforementioned crystal structures are displayed in Figure 3 [15].

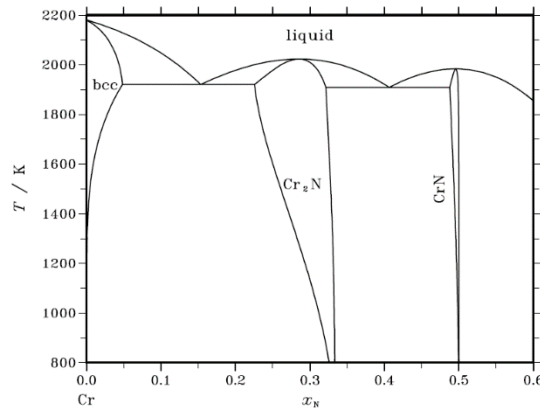


Figure 2: Cr-N equilibrium binary phase diagram [14].

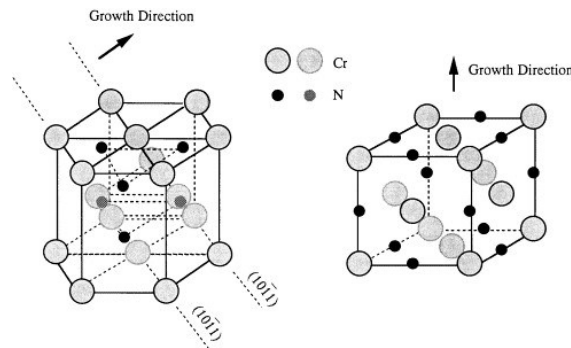


Figure 3: crystal structures in the Cr-N system [15].

## AlN

AlN is a covalent nitride with a high thermal conductivity and a high electrical resistivity. These properties, combined with high strengths and a thermal expansion coefficient similar to Si, make the material interesting for the electronics industry [12].

The Al-N equilibrium binary phase diagram is illustrated in Figure 4, it contains only the stable wurtzite-structured AlN [16].

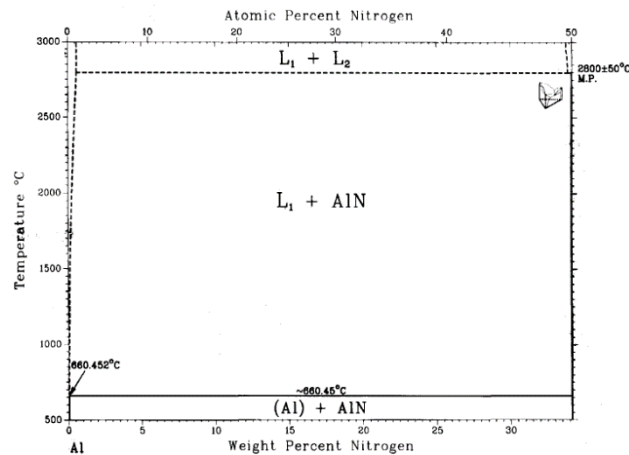


Figure 4: Al-N equilibrium binary phase diagram [16].

Nevertheless, AlN exists in three different crystal structures: The stable wurtzite structure and two metastable cubic structures, the B1 rocksalt structure and a zincblende structure (Figure 5). The rocksalt structure is stable at pressures above 15-20 GPa in bulk form. Zincblende structured AlN is metastable at all pressures. In thin films, cubic rocksalt AlN can be stabilized for thicknesses of several lattice spacings by epitaxial growth on cubic structured substrates or template layers with a close lattice parameter match. The thickness of B1 AlN is limited to only a few nanometers [17].

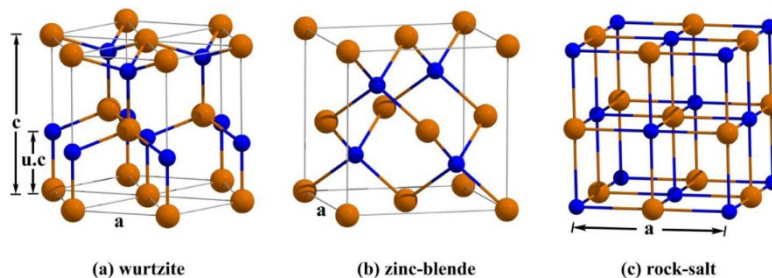


Figure 5: different crystal structures of AlN [58].

### 2.1.3. CrN/AlN SL coatings

CrN/AlN SL coatings exhibit good mechanical properties and oxidation resistance. Applications are: protective coatings for forming tools, cutting tools and other parts that are exposed to high thermal and mechanical loads [6,18].

#### **Stabilization of the metastable B1 structure of AlN in CrN/AlN SL coatings:**

A special feature of these coatings is the stabilization of cubic rocksalt B1 AlN in CrN/AlN SL coatings [18]. Stabilization of metastable B1 cubic AlN at ambient pressures in SL structures is possible if the lattice constants of cubic phases are similar and the layer thicknesses remain below a critical value [18–20]. In the case of CrN/AlN SL coatings, the critical layer thickness of AlN is about 3 nm, and CrN layers must be at least as thick as the AlN layers [18,21].

A model for the critical layer thickness of AlN depending on the crystallographic orientation was introduced by Chen et al [21]. It is based upon an energy approach, which stated that the total energy is dependent on following energy contributions:

- Bulk energy
- Coherency strain energy
- Surface energy
- Interface energy

Contributions of bulk energy and coherency strain energy increase linearly with increasing layer thickness, and both are higher in cubic AlN than in hexagonal AlN. Surface energies can be higher, similar, or smaller, and interface energies are always smaller in cubic AlN compared to hexagonal AlN grown on a cubic template layer. Consequently, at small layer thicknesses - up to the critical thickness at which the total energies of cubic and hexagonal crystal structures are equal - cubic AlN is energetically more favorable (Figure 6).

Except of the bulk energy, all energy contributions are dependent on the crystallographic orientation of AlN and the orientation relation between AlN and CrN. Different energy contributions for different orientations also lead to different critical thicknesses. While for the (111) growth orientation a small critical thickness of 2 nm was observed, other orientations of the

cubic phase form up to higher thicknesses of 4.1 nm. For more details, the reader is referred to the original work [21].

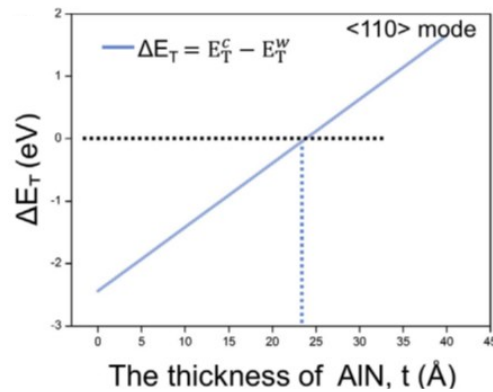


Figure 6: schematic illustration of the total energy difference ( $\Delta E_T$ ), which is the difference between the total energy of cubic B1-AlN ( $E_T^C$ ) and hexagonal B3-AlN ( $E_T^W$ ) [21].

## 2.2. Deposition of SL films via reactive magnetron sputtering

Nonequilibrium techniques are used to produce SLs. Combined materials nucleate and grow alternately on top of each other, deposition conditions are determinative for the structure [5].

### 2.2.1. Sputter deposition

Sputtering is a typical deposition method for thin films, which can be classified as a physical vapor deposition (PVD) method. PVD is a collective term for film deposition methods, where a solid or molten target material is evaporated by a physical mechanism [22,23]. Emitted atoms usually cross a reduced pressure environment to a substrate, where they condense, and form a film [22].

Sputtering is a plasma-assisted process, where a target material serves as cathode and a substrate serves as an anode [22,24]. Between the electrodes a working gas, usually argon, is introduced into the evacuated chamber [22,23]. Electrons moving towards the anode can ionize gas particles from the working gas, if they possess enough energy. As the formed  $Ar^+$ -particles are charged, they accelerate toward the target (cathode) [25]. This event is called gas discharge and is the reason that a current flows through the gas and the substrate [22]. At low pressures of typically 2-20  $\mu$ bar, ions with high energies and momentum bombard the target [25]. Due to a momentum transfer, atoms are ejected from the target material [22,24]. Also, other particles like secondary electrons, desorbed gas, negative ions, and radiation are emitted. Target material atoms cross

the discharge area and deposit on the substrate [22]. Figure 7 illustrates a simple sputtering configuration with one target [23].

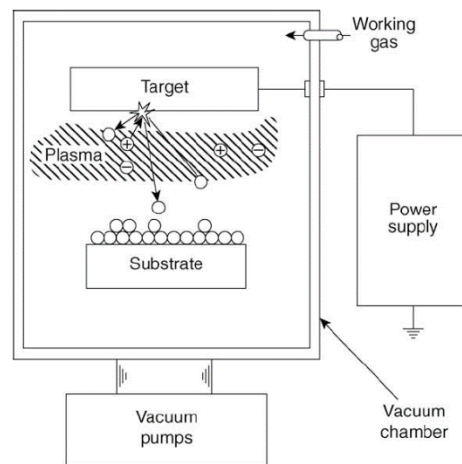


Figure 7: schematic representation of a sputtering process [23].

A negative voltage, the so-called bias voltage, can be applied to the substrate (anode). This results in ion bombardment of the growing film, and thereby leads to some beneficial effects [26], like densification of the film by an increased adatom mobility and formation of compressive residual stresses [27].

### Sputter modes

Regarding the type of applied voltage on the electrodes, one can distinguish between different sputter modes:

- DC sputtering: A constant negative voltage is applied to the target (cathode). It is applicable on conductive target materials and, during reactive sputtering insulating compound films can be formed on the target surface [24].
- Pulsed DC sputtering: Negative and positive pulses alternate with a certain frequency. This solves the above-mentioned problems with DC sputtering - positive pulses neutralize the positive charge by electron bombardment. Furthermore, additional parameters, like pulse width, pulse frequency and duty cycle lead to more opportunities in parameter-choice. Typical pulsing frequencies are  $\geq 100$  kHz [24].
- RF sputtering: Typically, a frequency of 13.56 MHz is used [24]. It can be used for insulating and conductive targets and films [22,24]. A disadvantage is the commonly low deposition rate [22].

## Magnetron sputtering

In magnetron sputtering, magnets below the targets generate a magnetic field. This makes sputter processes more efficient, because electrons are trapped near the target and ionization rate is higher in this area. Two different magnetron configurations and following two different alignments of magnetic fields are possible. Figure 8 displays the balanced magnetron configuration, where magnetic field lines are closed, and the unbalanced magnetron configuration, where some magnetic field lines are oriented towards the substrate. The second configuration has the advantage of densifying the ion and electron density also near the substrate [25]. As a result, electrons and ions can bombard the growing film and a dense film can be obtained [28].

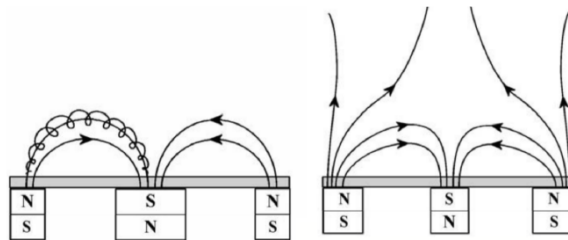


Figure 8: balanced and unbalanced magnetron configurations [25].

### 2.2.2. Reactive sputtering

Non-metallic films can be deposited with metal targets and a reactive gas additionally to the inert gas [22]. A gas mixture is chosen because reactive gas atoms are very light compared with argon and would not be very successful in ejecting target atoms while bombarding the surface. Usually, nitride films are deposited by reactive sputtering, but also oxide, oxynitride, carbide and sulfide films can be produced. Reactive gas atoms react with the target material on the substrate or the target [28]. Reactions during the gas transport are unlikely, because a third species is needed to get rid of the redundant energy [25]. Above a critical gas flow a compound film emerges on the target and a nearly stoichiometric film is sputtered [28].

### 2.2.3. Film formation and structure zone model

The three different growth modes in film formation are: 3D-island growth (Vollmer-Weber), layer-by-layer growth (Frank-van der Merve) and the combined growth mode where layer is followed by island growth (Stransky-Krastanov) [28]. Under near-equilibrium conditions surface energies and interface energies determine the occurring growth mode. Considering the SL structure which

consists of nm thin layers, the layer-by-layer growth is the preferential mechanism to obtain planar layers [5].

As thin films are usually deposited under non-equilibrium conditions, process parameters are decisive for film properties, which can vary widely. Particularly the deposition temperature and energetic particle bombardment have a crucial impact on film structure and properties. Structure zone models were developed to describe the structure of films as a function of the deposition parameters [28]. Different structure zone models were developed. The structure zone model by Barna et al. suggested the film structure development in dependence of the homologous temperature [29]. Thornton [30] introduced a second axis, which considers the influence of the argon gas pressure. Anders suggested another SZM [31], it is displayed in Figure 9. The two input parameters are the generalized temperature  $T^*$  and the normalized energy flux  $E^*$ . The generalized temperature is the sum of the homologous temperature and the temperature change due to potential energies of incoming particles. The normalized energy flux describes the influence of the kinetic energy of bombarding particles [31].

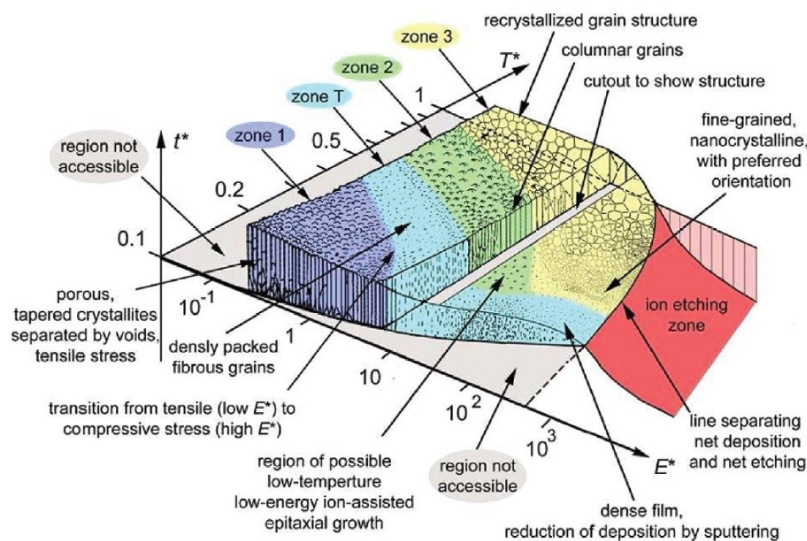


Figure 9: Structure zone model by Anders [31].

With a look at important factors for SL film deposition, the main influences of the main parameters are:

**Temperature:** In general, increasing the substrate temperature enhances the adatom mobility during film growth [32]. For SL films, low temperatures (zone 1), which results in porous structures with surface texture and nonuniform layers due to the missing surface texture, should



be avoided. Also, too high temperatures (zone 3), where bulk diffusion predominates, is not optimal for interface properties. In the remaining intermediate temperature region, surface diffusion is dominating and dense columnar structures with flat surfaces develop. Additionally, the structure of the substrate or the latest deposited layer influence the growth and crystallographic orientation of the emerging layer. To obtain layer growth instead of island growth for both alternating materials keeping the surface diffusion little by using rather small homologous temperatures between 0.20 and 0.35 is expedient [5].

**Pressure:** Pressure has a strong impact on film structure, as it controls the probability of sputtered particles colliding with gas during their transport to the substrate. High pressures result in many collisions which reduce energies of sputtered particles during their transport to the substrate [31].

**Bias voltage:** Biasing the substrate holder is realized by applying a negative potential. Consequently, positively charged energetic particles bombard the growing film [28]. This usually results in an enhancement of adatom mobility, as energy is transferred to the adatoms. Consequently, the film densifies, the film surface and layer surfaces smoothen, and the crystallographic orientation is influenced [5,27]. Additionally, some particles are implanted in the film. This also densifies the film and causes residual compressive stresses [27]. Beside these positive effects, the increased adatom mobility is not necessarily beneficial for depositing SL films, because along with the higher adatom mobility, diffusion rates also increase and intermixing at interfaces is promoted [5].

### 2.3. Mechanical properties of SL films

Concerning the response of a solid material to an applied stress, one can differentiate between elastic and plastic material behavior. Elasticity means that a solid material returns to its unstrained state as the stress is removed, while for plastic deformation a permanent deformation remains after removal of the stress. For brittle materials, plastic deformation usually only occurs at high temperatures, or under special circumstances, as for example during hardness testing. At low temperatures, elastic deformation followed by brittle fracture can be assumed [33].

The hardness of a material is defined as its resistance to local plastic deformation [22]. Interatomic forces and crystal structure are decisive for the intrinsic hardness of a material. Additionally, the microstructure of the material has a decisive influence on hardness [28].

Mechanisms which strengthen the material by decreasing the dislocation mobility result in an increase in hardness. Generally, the following strengthening mechanisms can be distinguished: solid solution hardening, particle hardening, work hardening and boundary strengthening [34].

In thin films many point and line defects, as well as boundaries between grains, phases and columns can be present. Also, second phase particles and solutes can act as obstacles for dislocation movement [2].

Hardness enhancement in SL films occurs because interfaces between two coherent layers with different shear moduli are obstacles for dislocation movement. With a raise of the shear modulus difference, the energy barrier for dislocations moving from the material with lower shear modulus to the material with higher shear modulus increases [35].

### 3. Experimental details

#### 3.1. Film fabrication

Films were deposited with an AJA ATC-1800 UHV sputtering system via reactive unbalanced magnetron sputtering. Details on the deposition system, the substrate preparation and the deposition parameters are presented in the following.

##### 3.1.1. Deposition setup

The vacuum chamber is equipped with four magnetrons, each is powered by a generator, which can be operated in DC or pulsed DC mode. For biasing, two generators can be connected to the substrate holder. One can be operated in DC or pulsed DC mode, the other is used for RF-biasing. In the present series of depositions, always DC-biasing was chosen. For depositions Cr (99.95% purity) and Al targets (99.99% purity) with a diameter of 3 inches were used. If two targets of each material were used, the same targets were mounted opposite to each other. When only one target was used, the Cr target was installed at “position 1” and the Al target at “position 3”. Above the targets movable shutters were mounted to fully cover the targets when closed. For all depositions, the target-to-substrate distance was set to 100 mm and the targets were tilted to the maximum possible tilt angle. Rotation speed was set to approximately 0.5 Hz.

##### 3.1.2. Substrate preparation

###### Preparation for deposition

Before the deposition, the vacuum chamber was evacuated for a few hours to obtain a base pressure below  $10^{-3}$   $\mu\text{bar}$ .

Substrates and dimensions of substrates were:

- Silicon (Si) (100) substrates: 20 mm x 7 mm,
- Magnesium oxide (MgO) (100) substrates: 10 mm x 10 mm, and
- Austenitic stainless-steel substrates: 28 mm x 10 mm.

Si (100) substrates, steel substrates, and MgO (100) substrates were ultrasonically cleaned in acetone and alcohol for a minimum of 5 minutes each. Subsequently, all substrates were mounted on the substrate holder (Figure 10). After the substrates were positioned above the

targets and the substrate-to-target distance was adjusted, the chamber was heated up to 550°C with a heating rate of 2 K/s for about 30 minutes.

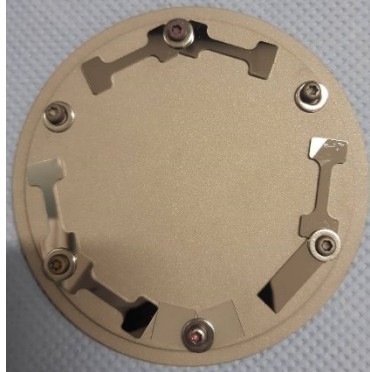


*Figure 10: arrangement of substrates on the substrate holder.*

### **Polishing of austenitic stainless-steel substrates**

Steel substrates were glued with epoxy resin onto the sample holder and polished with STRUERS Prepatic-2 fully automatically with the predefined program “Austenite”. Polishing took place in four approximately 10-minutes long steps with intermediate cleaning before the substrates were moved to the next polishing plate with a finer polishing paste grain size each time. In the last step, substrates were polished with diamond paste of 1  $\mu\text{m}$  grain size for 10 minutes.

### **3.1.3. Film deposition**

The deposition processes were prepared via Excel files “AJA Remote process emulator” and contained all following preparation steps, as well as the deposition itself and a ramp-down step.

### **Substrate etching and pre-sputtering**

The first steps were the same for all films deposited. First, the pressure was set to 30  $\mu\text{bar}$  with a substrate voltage of -550 V. Subsequently, the chamber pressure was ramped down to 2  $\mu\text{bar}$ , while the argon flow rate was set to 20 sccm and bias to -550 V with pulse frequency of 100 kHz. As next step, the substrates were etched in argon atmosphere and the targets were pre-sputtered for 5-10 minutes at 500 °C and 2  $\mu\text{bar}$ . For pre-sputtering, the target powers were set to the same value as later used for the film deposition and all shutters remained closed. For ion etching of the substrates, simultaneously a bias of -700 V with a pulse frequency of 100 kHz was applied. For SL

coatings, an “interlayer” between substrate etching and deposition was added, in which all parameters were set to deposition conditions, but the shutters remained closed for 10 seconds.

### Film deposition

Deposition parameters for the final set of films are summarized in Table 1:

*Table 1: Deposition parameters.*

	AlN	CrN	CrN/AlN 4/2 [nm]	CrN/AlN 4/5 [nm]
Temperature [°C]	500	500	500	500
Pressure [μbar]	2	2	-	-
Position of the VAT valve	-	-	518*	518*
Bias [V]	-70	-70	-70	-70
Ar flow rate [sccm]	10	8	8	8
N <sub>2</sub> flow rate [sccm]	20	12	12	12
Power Al [W]	500 · 2	0	500 · 1	500 · 1
Power Cr [W]	0	300 · 1	300 · 1	500 · 1
Layer time Al [s]	9940	0	15	48
Layer time Cr [s]	0	6960	19	19
Number of layers	1	1	561	161

\* Corresponds to about 2.0-2.3 μbar

All targets were powered in pulsed DC mode with a pulse frequency of 100 kHz and a pause duration of 1 μs. Bias voltage was set to DC mode in the deposition layers.

In SL coatings, the first CrN layer was set to 30 s. With exception of the layer time, which alternated layer-wise, parameters were kept constant during the whole process. Deposition of alternating materials was realized with mechanical shutters. The pressure of 2 μbar was indirectly adjusted by the position of the VAT valve. In position mode, the pressure varied between 2.0 and 2.3 μbar during all SL depositions.

### 3.2. Structure analysis

Structure analyses with X-ray diffraction were carried out with Bruker-AXS D8 Advance and Bruker-AXS D8 Advance da Vinci diffractometers using CuK<sub>α</sub> radiation. XRD patterns were measured in a 2θ range of 30-85°. On both devices, a step size of Δ2θ = 0.02° and a measurement time of 1.2 seconds per step were chosen.

XRD-patterns of all films were measured with the Bruker diffractometer Advance. For a better quality of the satellite peaks of the SL films, films were measured with the Bruker-AXS D8 Advance da Vinci. With this device also  $\text{CuK}\beta$  and  $\text{WL}\alpha$  peaks were measured. They were removed from the recorded diffraction pattern with the software TOPAS [36]. TOPAS was also used to determine peak positions and satellite peak positions in patterns of the SL coatings.

### **3.3. Film thickness measurement**

Film thickness was measured with the laser confocal microscope Keyence VK-X1000. To determine the film thickness, the height difference between substrate and film was measured. The substrate was set as reference plane and the height difference were measured via a “profile” and an “average-height-difference” measurement. Optical images of crack patterns in monolithic CrN films were also taken with this device.

### **3.4. Measurement of hardness and Young’s modulus**

Hardness measurements were performed with UMIS nanoindenter. Before the measurement, the samples were glued onto the sample holder with epoxy resin and put in the indentation chamber at least three hours before the measurement. Indents were done with a Berkovich diamond tip, and the hardness values were evaluated with the corresponding area function. The Poisson’s ratio was set to 0.22 for CrN, 0.28 for AlN and 0.25 for the SLs [37]. 41 Indents were made per sample in a load range from 2.5 to 22.5 mN. At each indent, a load displacement curve was recorded, and values for hardness and Young’s modulus were automatically calculated via the Oliver and Pharr method [38] for each indent. To minimize the influence of the substrate, only indentation depths <10% of the film thickness were used for the evaluation.

## 4. Results and discussion

This chapter correlates film synthesis parameters with the structural and mechanical properties of CrN- and AlN-based monolithic and SL coatings. It will be discussed how the deposition parameters have to be set in order to obtain films with the desired properties. Subsequently, results of structural and mechanical film characterizations on different substrates will be presented.

### 4.1. Film deposition

The deposition parameters, which result in coatings with the desired properties, depend on the film material systems and the deposition system used. Therefore, a suitable parameter set had to be found. Trends and results from preliminary depositions are presented in the following. Subsequently, the final process parameters chosen are summarized.

#### 4.1.1. Deposition parameter study

The SL structure consists of nanometer thin layers which are grown consecutively on top of each other. The coating time of the individual layers is only a few seconds, due to the small layer thickness. As also the time for switching from one layer material to the other should be as short as possible to avoid excessive surface contamination by impurities, such as oxygen, it is advisable to keep most coating parameters constant for both target materials used. Hence the searched-for parameters, such as the total pressure, the gas flows of Ar and N<sub>2</sub>, and the bias voltage have to be suitable for both materials that are combined in a SL structure. The only difference between process parameters can be the target power.

#### Required properties of CrN and AlN

CrN serves as template layer for the epitaxial stabilization of B1-structured AlN. It is therefore important to provide enough nitrogen during the deposition so that single-phased B1-structured CrN forms. Consequently, the formation of Cr<sub>2</sub>N, which occurs if nitrogen availability is too low, must be avoided. For that reason a low Ar : N<sub>2</sub> ratio and a low Cr target power are expedient. In addition, CrN should not grow with a preferred crystallographic growth orientation of 111 since the critical thickness for complete stabilization of AlN in the B1 structure is then lower than if differently oriented CrN template layers were used [21]. The preferred crystallographic

orientation of CrN can be adjusted via the deposition parameters. Other requirements are a dense film structure and a reasonable hardness of CrN and AlN films. Also, an amorphous structure of AlN (which was found to occur at high nitrogen contents) should be avoided.

### **Investigated parameter range**

In all deposition runs, the deposition temperature was set to 500 °C and the chosen bias voltage was -70 V. The total gas pressure of Ar and N<sub>2</sub> was varied between 2 and 5 μbar, the gas flow rates were 7-20 sccm with Ar/(Ar+N<sub>2</sub>) fractions of 26 – 40 %, and the target power 250–500 W. The parameters were set within the above stated variation ranges and their influence on the film properties was investigated.

The deposition parameters reported in earlier work for CrN- and AlN-based coatings [21,39–41] were used as starting parameters. However, this led to comparatively poor mechanical properties. Only the reduction of the total pressure from 4 μbar to lower values resulted in a significant improvement of the film properties. This can be seen in Figure 11, which shows an increase in hardness and Young's modulus of CrN coatings with decreasing total gas pressure. However, it should be mentioned that the test films were sometimes quite thin and, in addition to the overall pressure, other parameters were also varied at the same time (see legend to Figure 11). The results should therefore be considered qualitative rather than quantitative. The influence of the total pressure on the film structure was shortly discussed in Sect. 2.2.3 of this work where reference to Thornton's structure zone model was given [30]. Similar to the results of this work, Daniel et al. previously reported the formation of a denser microstructure and superior mechanical properties for TiN coatings synthesized in the same deposition system as used here when low gas pressure was used [32]. From this it can be concluded, that it is advantageous to choose a low total gas pressure, resulting in less scattering of energetic sputtered target atoms, in order to achieve good mechanical film properties.



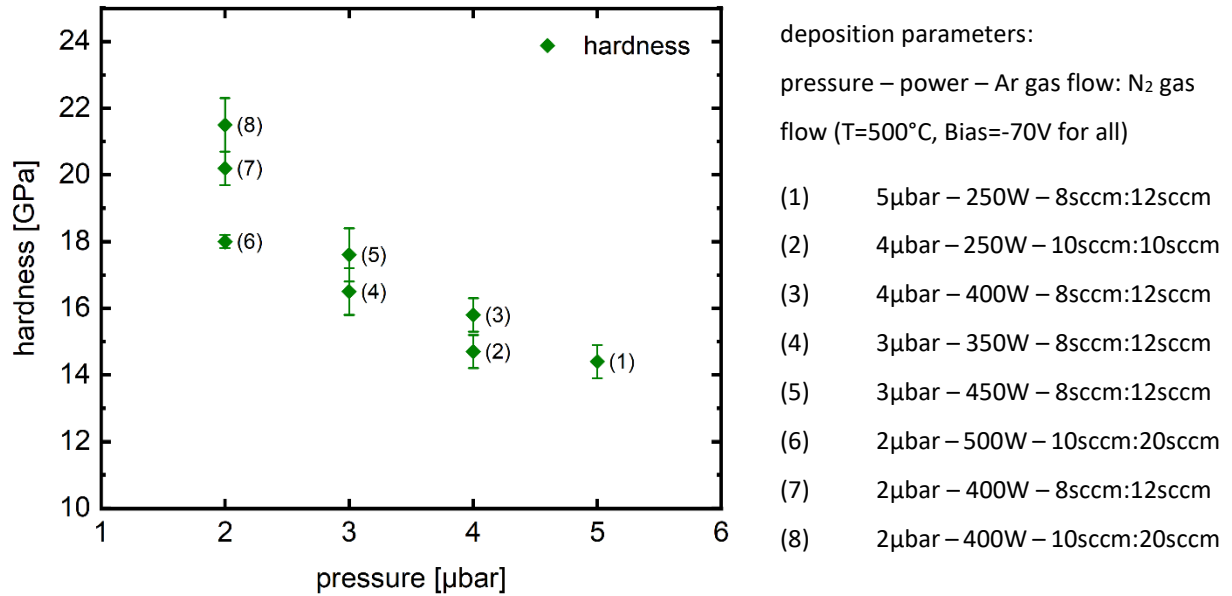


Figure 11: hardness of CrN films in dependence of the total gas pressure.

#### 4.1.2. Final parameter choice

The final deposition parameters, which were selected based on the analysis of the results of the systematic parameter study, are summarized in Table 2.

Table 2: final process parameters chosen for the layer materials.

	AlN	CrN
Temperature [°C]	500	500
Pressure [μbar]	2	2
Bias [V]	-70	-70
Ar flow rate [sccm]	8	8
N <sub>2</sub> flow rate [sccm]	12	12
Power Al/Cr [W]	500 ·1	300 ·1

Except of the target powers, all parameters are the same. A trade-off between a high nitrogen partial pressure needed so that CrN crystallizes in the single-phase cubic-structure and a low enough nitrogen partial pressure to obtain crystalline (and not amorphous) AlN was found in the Ar : N<sub>2</sub> ratio of 8 : 12. To avoid amorphous AlN formation, the Al targets were run at a higher power which resulted in an increased nitrogen consumption, while the lower power set for the Cr target kept the nitrogen consumption low, thereby avoiding the formation of Cr<sub>2</sub>N and at the same time the promotion of the formation of the desired crystallographic 100 orientation.

#### 4.1.3. Critical layer thickness of monolithic CrN

Cracks were observed in some monolithic films deposited on Si (100) substrates. This film damage occurs due to tensile residual stresses in the film, if a critical film thickness is exceeded [28,42]. To determine the critical film thickness at which cracks form, CrN was deposited three times, each time with a different film thickness but otherwise with the same deposition parameters. At a layer thickness of 1.70  $\mu\text{m}$ , many cracks and short crack spacing were observed (Figure 12 (a)). At a lower film thickness of 1.47  $\mu\text{m}$  (Figure 12 (b)), the distance between cracks increased noticeably, and no cracks were detectable in 1.40  $\mu\text{m}$  thick films. As shown in Figure 13, the critical film thickness is expected to be in the range between 1.40 and 1.47  $\mu\text{m}$ .

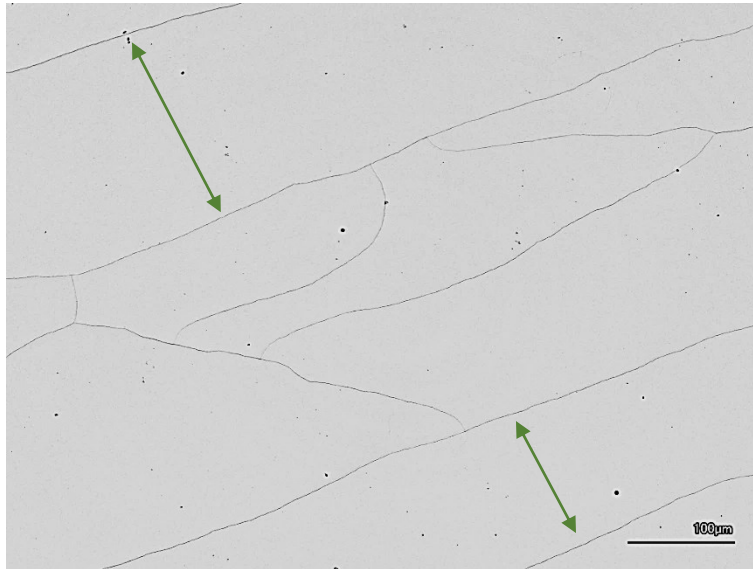


*Figure 12 (a): laser confocal optical microscopy (LCOM) image of the crack pattern at 1.70  $\mu\text{m}$  film thickness.*

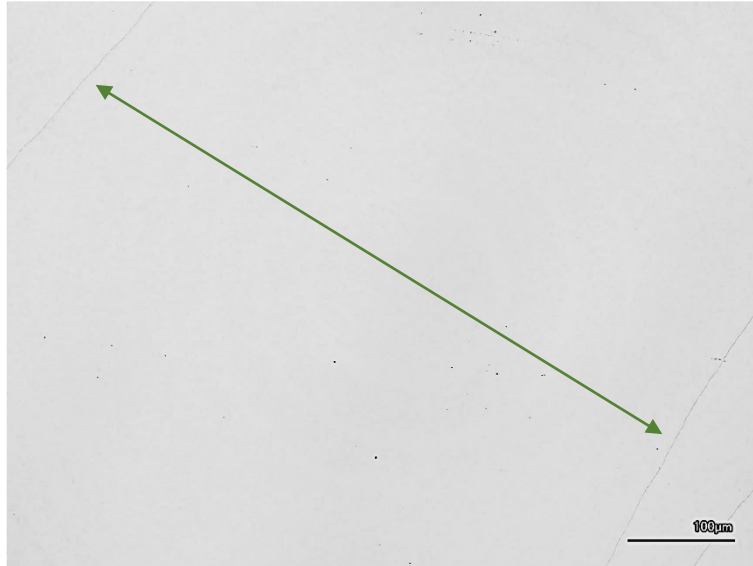


Figure 12 (b): LCOM image of the crack pattern at 1.47  $\mu\text{m}$  film thickness.

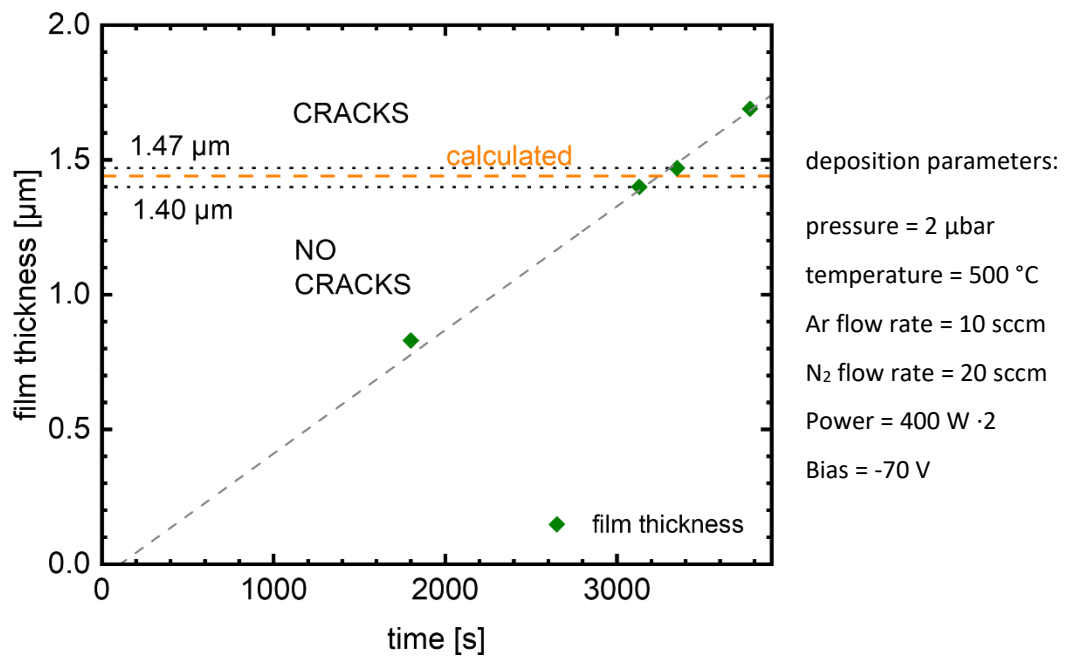


Figure 13: critical film thickness of CrN on Si (100) substrate.

The residual stress state is mainly determined by the contributions of growth stresses, thermal stresses and bombardment-induced stresses, which are generated during film deposition. Thermal stresses occur with temperature changes because the thermal expansion coefficients of film and substrate do not match [27]. If the thermal expansion coefficient of the film is higher than that of the substrate, tensile stresses develop in the film upon cooling down from deposition temperature to room temperature [43].

This is the case for CrN films on Si (100) substrates, as the thermal expansion coefficient is with  $\alpha_{CrN} = 7.5 \cdot 10^{-6} \text{ K}^{-1}$  lower than that of  $\alpha_{Si} = 3.55 \cdot 10^{-6} \text{ K}^{-1}$  [44]. The resulting biaxial stress  $\sigma_m$  can be calculated with the following formula [43]:

$$\sigma_m = \frac{\Delta\alpha \cdot \Delta T \cdot E_F}{(1-\nu_F)} = 7.48 \cdot 10^8 \text{ Pa} = 748 \text{ MPa} \quad (1)$$

$\Delta\alpha$  is the difference in thermal expansion coefficients ( $\Delta\alpha = 3.95 \cdot 10^{-6} \frac{1}{\text{K}}$ ),  $\Delta T$  is the difference between deposition temperature ( $T_0 = 500 \text{ °C}$ ) and room temperature ( $T_r = 22 \text{ °C}$ ),  $E_F$  is the Young's modulus of the film, which was measured by nanoindentation ( $E_F = 309 \text{ GPa}$ ), and  $\nu_F$  is the Poisson's ratio ( $\nu_F = 0.22$  [37]).

For a given stress  $\sigma$ , a critical film thickness  $h_c$ , above which a through-the-thickness crack is energetically favorable, can be calculated [42,43,45]. It depends on the fracture resistance  $\Gamma$  ( $\Gamma = 4.9 \frac{\text{J}}{\text{m}^2}$  [46]), the Young's modulus of the film  $E_F$ , the Poisson's ratio  $\nu$ , the mismatch stress  $\sigma_m$  and a dimensionless driving force  $Z$ .  $Z$  depends on the crack pattern, for channel cracks  $Z = 1.976$  is applicable. It is assumed that Young's moduli of film and substrate are similar, and that the substrate is infinitely thick [43]. These values and assumptions result in the following critical film thickness (plane strain):

$$h_c = \frac{\Gamma \cdot E_F}{Z \cdot (1-\nu^2) \cdot \sigma^2} = 1.44 \cdot 10^{-6} \text{ m} = 1.44 \text{ }\mu\text{m} \quad (2)$$

The calculated critical thickness of  $1.44 \text{ }\mu\text{m}$  is located between the two experimental thicknesses, which enclose the critical thickness (Figure 13). Nevertheless, it is only an approximation. The actual value for the fracture resistance is not known precisely for this film. Additionally, Young's moduli of Si and CrN are not similar. The Young's modulus of CrN is higher than that of Si, which would increase the Z-factor [47]. Simultaneously, the tensile stress present in the film is likely to be overestimated because deposition with substrate bias usually introduces compressive residual stresses into the film [27], which superimpose the tensile thermal stresses.

#### 4.1.4. Deposition of SL films

##### Architectures

SL coatings with different layer thicknesses were produced: SLs where AlN was fully stabilized in the cubic structure and SLs which contained cubic and hexagonal structured AlN. To obtain single phase cubic structured AlN, the CrN template layers have to be at least as thick as the AlN layers and the AlN layers must not exceed a critical thickness [48]. The critical thickness for AlN to be fully stabilized in the cubic structure is dependent on the crystallographic orientation: about 4 nm when grown on 100 or 110 oriented CrN template layers and 2 nm for 111 [21]. A total film thickness of 1.5  $\mu\text{m}$  was aimed for.

##### Process features and shutter timing

To produce SL films, computer-controlled shutters above the targets opening and closing alternately were used. For an improved process stability, only one target of each material was used in the SL processes, and the deposition pressure was regulated via the position mode of the VAT valve.

Two different shutter timings were tested. One without pause between the different layers and a second, where both layers were closed for approximately 2 seconds after each layer. A comparison of similar films on MgO (100) produced with different shutter timings can be found in Figure 14. Difference in growth orientations, a lower measured hardness, and the fact that the appearance of hexagonal AlN could not be excluded, showed that the second approach with pauses between the layers is the better choice.

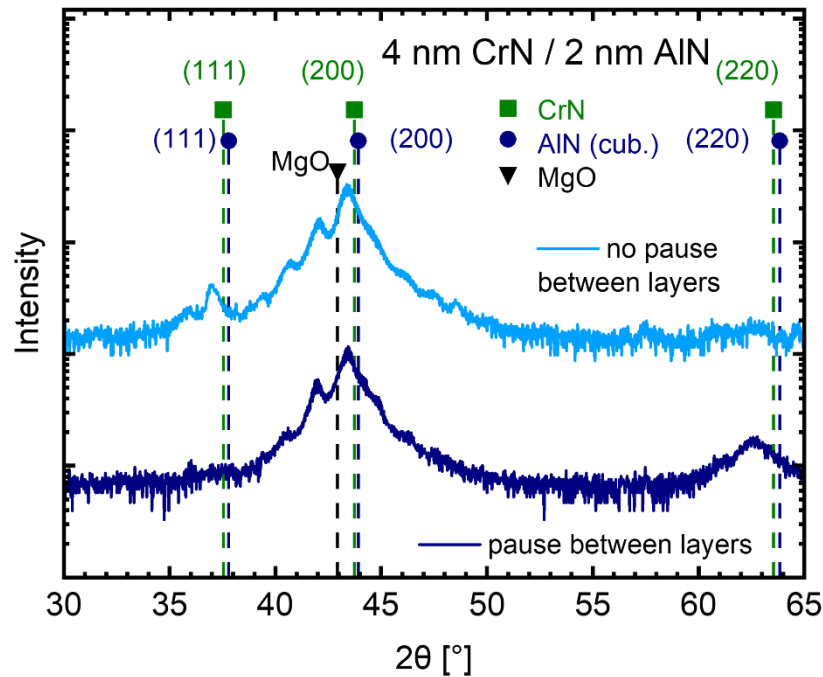


Figure 14: XRD patterns of films deposited with different shutter timing.

## 4.2. Film characterization

Finally, properties of the following films will be compared: Two different multilayer films, one with fully stabilized cubic AlN with a nominal architecture of 4 nm CrN / 2 nm AlN (CrN/AlN 4/2), and one containing also hexagonal AlN and a nominal architecture of 4 nm CrN / 5 nm AlN (CrN/AlN 4/5). Furthermore, results of monolithic CrN and AlN films complete the comparison.

### 4.2.1. Film structure

XRD analysis revealed the crystal structure, the preferred growth orientation and reflected the SL structure of the multilayer systems. Figure 15 and Figure 16 show the XRD-patterns of coatings on Si (100) and MgO (100). Brown patterns represent monolithic AlN and green patterns CrN films. AlN in its hexagonal structure was only deposited on MgO (100) substrate, since a film thickness of approximately 1.5  $\mu\text{m}$  was not possible on Si (100) substrate due to the low critical thickness for crack formation in AlN.

Blue patterns are the CrN/AlN SL coatings with a nominal architecture of 4 nm CrN / 2 nm AlN. Growth orientations are comparable with those of monolithic CrN. For CrN and cubic AlN from the SL structure, one peak can be observed instead of two separated peaks. Beside the main

peaks, on both sides, satellite peaks can be observed. Satellite peaks occur due to the periodicity of the layered structure [49]. Distances in  $2\theta$  between satellite reflections are equal and depend on the bilayer period  $\Lambda$ . Intensities are not equal on both sides of the Bragg peak due to a difference in scattering power. Scattering power is usually larger for the material with the larger lattice spacing and hence negative satellite peaks usually have higher intensities [5]. This is also observable in Figure 15 and Figure 16.

The 4/5 architecture is represented by the purple curve. On both substrates, the (00.2) AlN peak indicates the presence of hexagonal AlN.

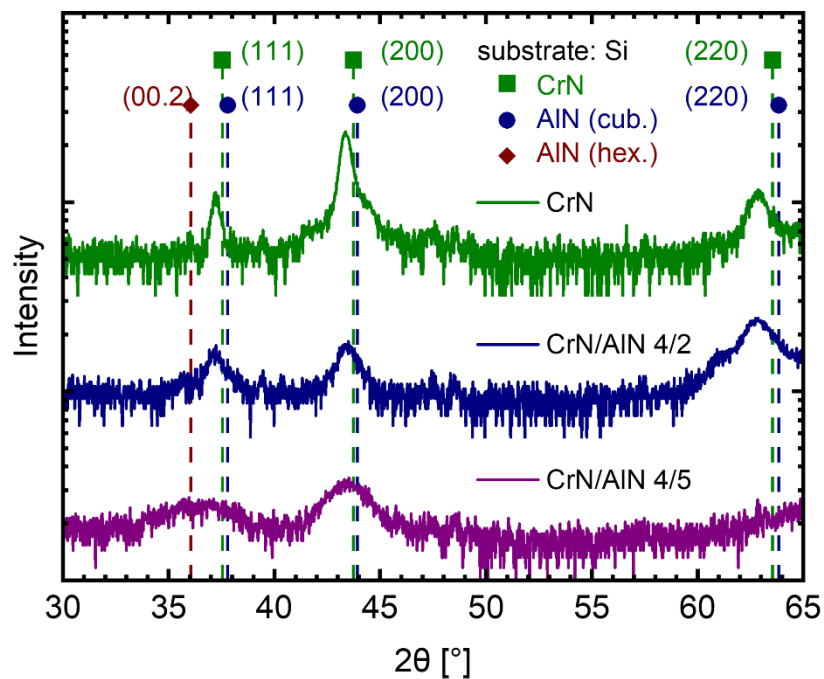


Figure 15: XRD patterns of different SL architectures on Si (100) substrates (JCPDF files: 11-0065 CrN, 25-1495 fcc AlN, 25-1133 hex. AlN).

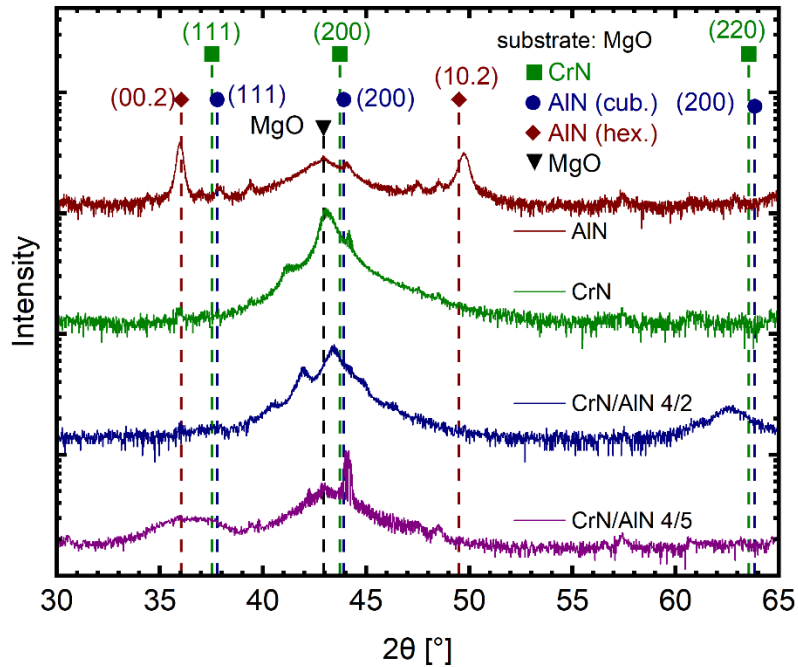


Figure 16: XRD patterns of different SL architectures on MgO (100) substrates (JCPDF files: 11-0065 CrN, 25-1495 fcc AlN, 25-1133 hex. AlN).

### Influence of the substrate

The underlying substrate determines whether single crystalline or polycrystalline films form [5]. On Si (100) with a native polycrystalline oxide scale, a polycrystalline film grows, while on MgO (100), a single crystalline film with the growth orientation of the substrates develops [50].

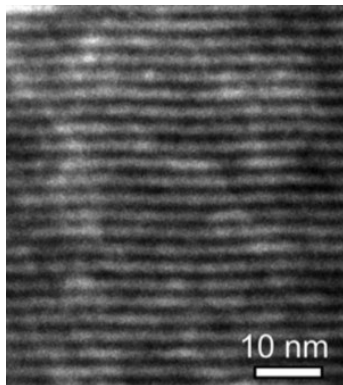


Figure 17: TEM image of a single crystalline SL film [50].

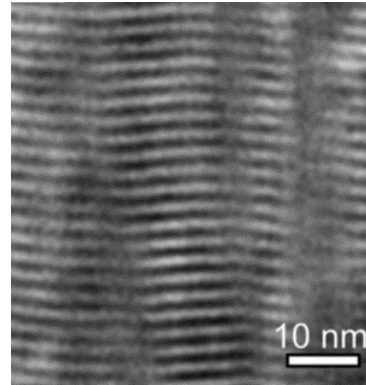


Figure 18: TEM image of a polycrystalline SL film [50].

In single crystalline SLs, no grain boundaries are existing within the individual layers, there are only planar layer boundaries, which separate the two materials. In comparison, lots of grain boundaries within the layers can be found in polycrystalline SLs. In each particular grain, the



following layer grows epitaxially and even. Consequently, a columnar grain structure over the collectivity of layers develops and, as observable in Figure 17 and Figure 18, due to the presence of grain boundaries layer interfaces become more curved [5].

X-ray diffraction patterns from monolithic CrN films are shown in Figure 19. As expected, a single crystalline film with 100 growth orientation is observed on MgO (100). On Si (100) a polycrystalline film forms (diffraction from differently oriented grains are detected).

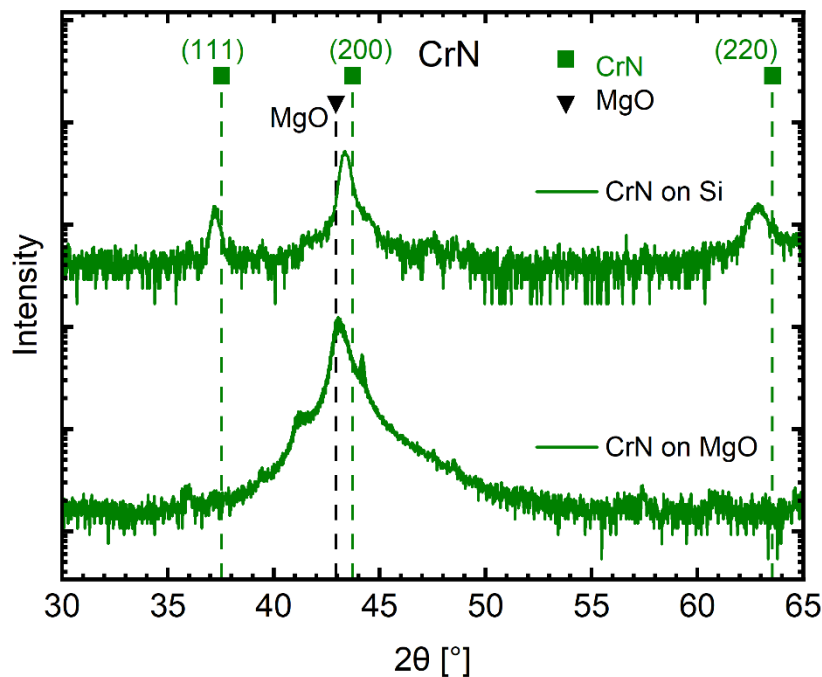


Figure 19: XRD patterns of CrN films on Si (100) and MgO (100) substrates (JCPDF files: 11-0065 CrN).

Films with 4/2 architecture have no preferred growth orientation on Si (100), a polycrystalline SL structure is formed (Figure 20). On MgO (100) almost only the 100 orientation is present again (logarithmic scale of plotted intensities).

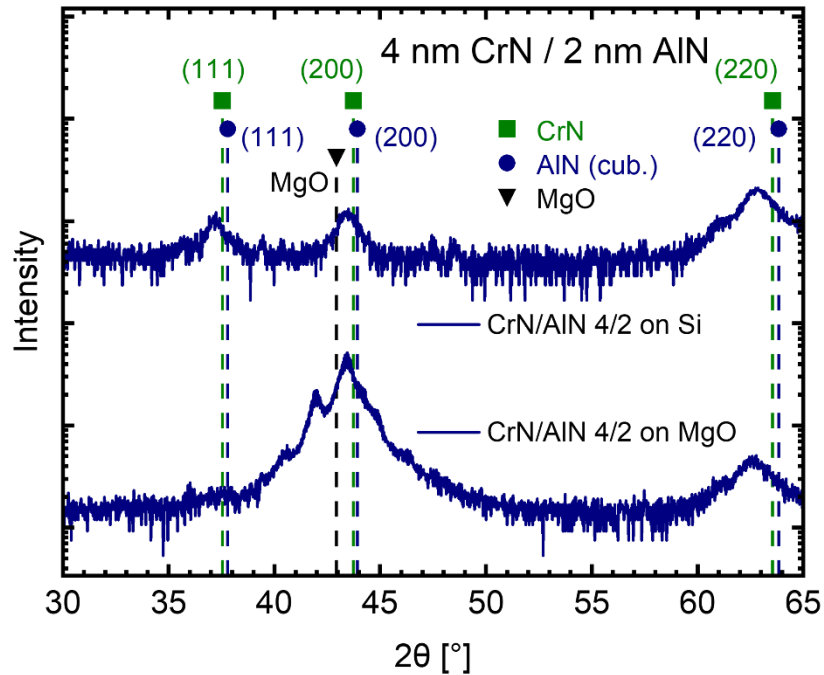


Figure 20: XRD patterns of 4 nm CrN / 2 nm AlN films on Si (100) and MgO (100) (JCPDF files: 11-0065 CrN, 25-1495 fcc AlN).

As also observable in Figure 20, on MgO (100), more satellite peaks (of higher order) with higher intensities are observable. The number and intensity of satellite peaks is dependent on the sharpness of the layer interfaces. An increase in number and satellite peak intensity suggests sharper interfaces in single crystalline CrN/AlN SL films deposited on MgO (100). This matches with the less planar layer interfaces expected for SLs on Si [5].

If AlN layers exceed the critical layer thickness, as it is the case for the 4 nm CrN / 5 nm AlN architecture, the epitaxial growth on MgO (100) cannot be maintained anymore. Due to the presence of hexagonal AlN, no clear structural difference between films on Si (100) and MgO (100) is observable in Figure 21.

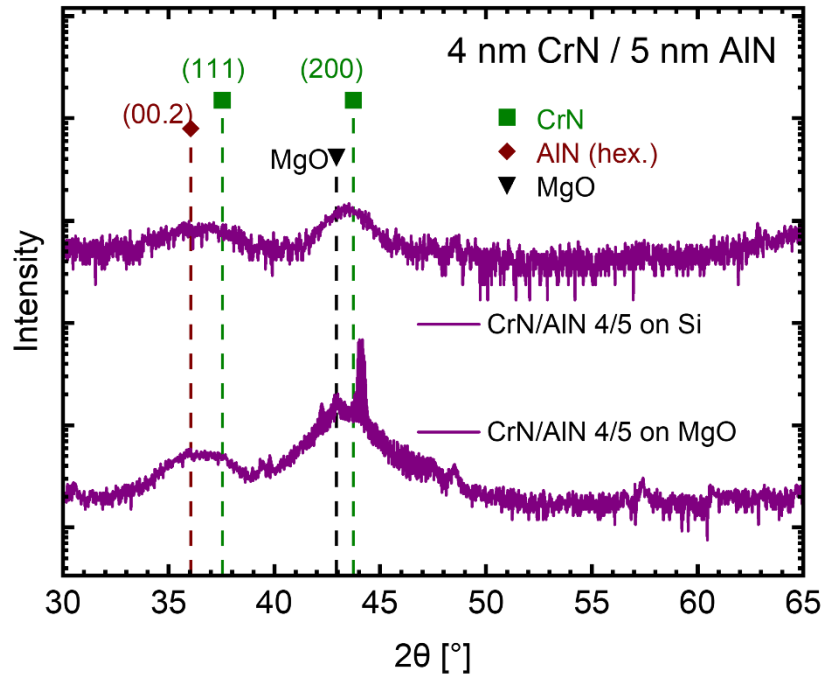


Figure 21: XRD patterns of 4 nm CrN / 5 nm AlN films on Si (100) and MgO (100) (JCPDF files: 11-0065 CrN, 25-1133 hex. AlN).

**Calculation of the bilayer periods**

Satellite peak positions give information about the bilayer period of SL films [51,52]:

$$\sin(\theta_{\pm}) = \sin(\theta_B) \pm \frac{\lambda}{2\Lambda} m \tag{3}$$

$\theta_{\pm}$  is the satellite peak position,  $\theta_B$  is the position of the Bragg peak,  $m$  is the order of the satellite peak,  $\lambda$  is the X-ray wavelength ( $\lambda = 0.154$  nm for CuK $_{\alpha}$ ) and  $\Lambda$  is the bilayer period.

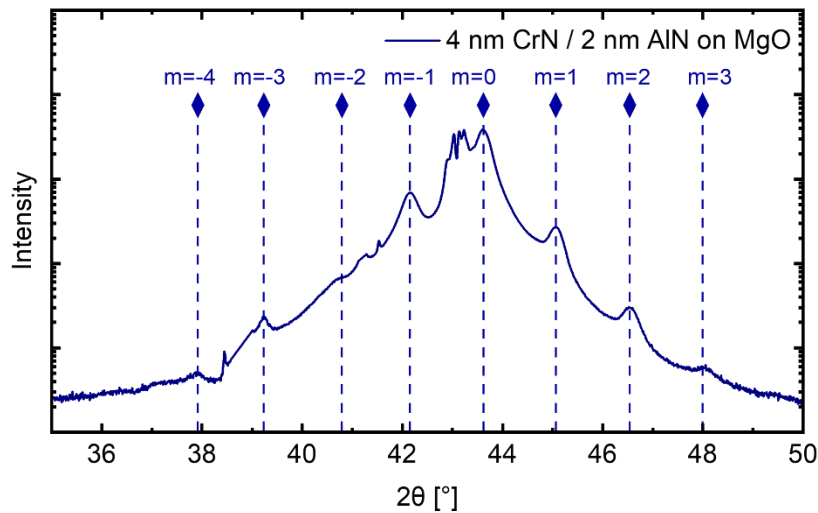


Figure 22: satellite peak positions of the 4 nm CrN / 2 nm AlN architecture on MgO (100) substrate.

Figure 22 shows the (200) peak of 4 nm CrN / 2 nm AlN films with surrounding satellite peaks and their positions on MgO (100). To calculate bilayer periods  $\sin(\theta_{\pm})$  values are plotted in Figure 23 in dependence of the order of satellite peaks. With formula (3) a Bragg peak position  $2\theta_B = 43.62^\circ$  and a bilayer period  $\Lambda = 6.6$  nm can be calculated.

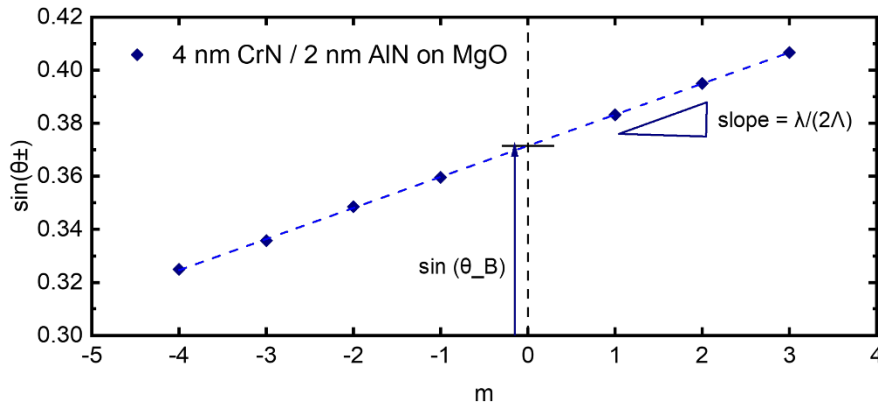


Figure 23: plot of satellite peak positions in dependence of their order  $m$ .

In Figure 24, the XRD pattern of the same SL film deposited on Si (100) is plotted. With measured positions of the (111) Bragg peak and the satellite peak with order  $m=-1$ , a bilayer period of 7.6 nm can be calculated.

Why the bilayer periods were larger in the SL films deposited on Si (100) compared to the films deposited on MgO (100) – even though they were synthesized in the same deposition run – could be a lower density in polycrystalline films and different deposition rates along different growth orientations.

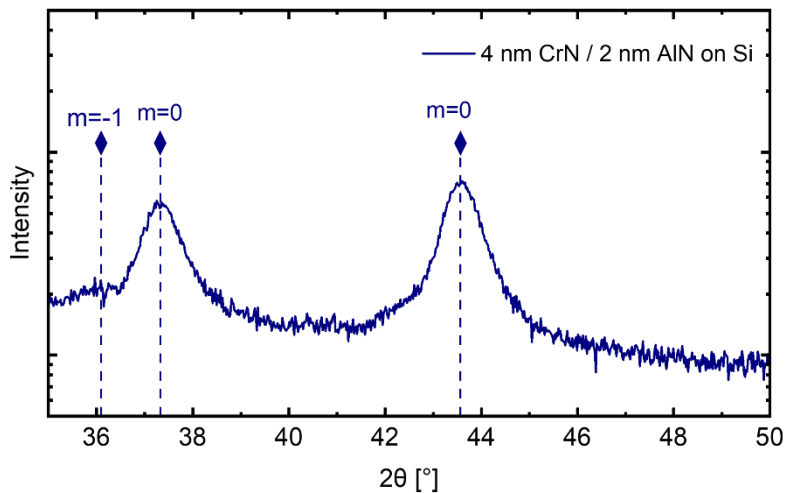


Figure 24: satellite peak positions of the 4 nm CrN/ 2 nm AlN architecture on Si (100).

#### 4.2.2. Film thickness and bilayer period

The total film thicknesses  $d$  are summarized in Table 3. The bilayer periods  $\Lambda$  were calculated from the total film thickness of the SLs on the different substrate types and the number of deposited layers.

Table 3: measured film thicknesses and calculated bilayer periods of monolithic and SL films

	Si (100)		MgO (100)		Austenitic stainless steel	
	$d$	$\Lambda$	$d$	$\Lambda$	$d$	$\Lambda$
	[ $\mu\text{m}$ ]	[nm]	[ $\mu\text{m}$ ]	[nm]	[ $\mu\text{m}$ ]	[nm]
CrN	1.38	-	1.30	-	1.29	-
CrN/AlN 4/2	1.67	5.9	1.45	5.2	1.33	4.7
CrN/AlN 4/5	0.71	8.7	0.69	8.4	0.53	6.5

Again, bilayer periods of single crystalline SL films on MgO (100) are lower than those of polycrystalline SL films on Si (100). It is noticeable, that bilayer periods calculated from XRD patterns are larger than those calculated from the total film thickness and the number of deposited layers. The difference could be explained by uncertainties in measuring the film thickness.

#### 4.2.3. Hardness and Young's modulus

Measured values for the hardness and Young's modulus of films on Si (100) and MgO (100) are summarized in Table 2 and plotted in Figure 25 and Figure 26.

Table 4: measured film thicknesses  $d$ , hardness  $H$  and Young's modulus  $E$  of different films on Si (100) and MgO (100) substrates.

	Si			MgO		
	$d$	$H$	$E$	$d$	$H$	$E$
	[ $\mu\text{m}$ ]	[GPa]	[GPa]	[ $\mu\text{m}$ ]	[GPa]	[GPa]
AlN	-	-	-	3.53	20.3 $\pm$ 1.7	327 $\pm$ 20
CrN	1.38	21.7 $\pm$ 0.9	309 $\pm$ 10	1.30	26.7 $\pm$ 0.7	377 $\pm$ 10
CrN/AlN 4/2	1.67	28.2 $\pm$ 0.7	314 $\pm$ 9	1.45	33.3 $\pm$ 1.3	393 $\pm$ 9
CrN/AlN 4/5	0.71	24.8 $\pm$ 1.0	246 $\pm$ 11	0.69	27.8 $\pm$ 1.0	336 $\pm$ 10

As can be seen, for the films on both substrate types, there is a hardness increase of about 6.5 GPa for the 4 nm CrN / 2 nm AlN SL film, compared with monolithic CrN. 4 nm CrN / 5 nm AlN films, which also contain hexagonal AlN achieve a significantly lower hardness than films with 4

nm CrN / 2 nm AlN architecture. This decrease can be attributed to the structural change and the higher bilayer period [53].

Young's moduli of 4 nm CrN / 2 nm AlN SL films, where AlN is stabilized in its cubic structure, obtain slightly higher values than monolithic CrN films. The Young's modulus of the 4 nm CrN / 5 nm AlN architecture, with portions of hexagonal AlN, is clearly below that of monolithic CrN films.

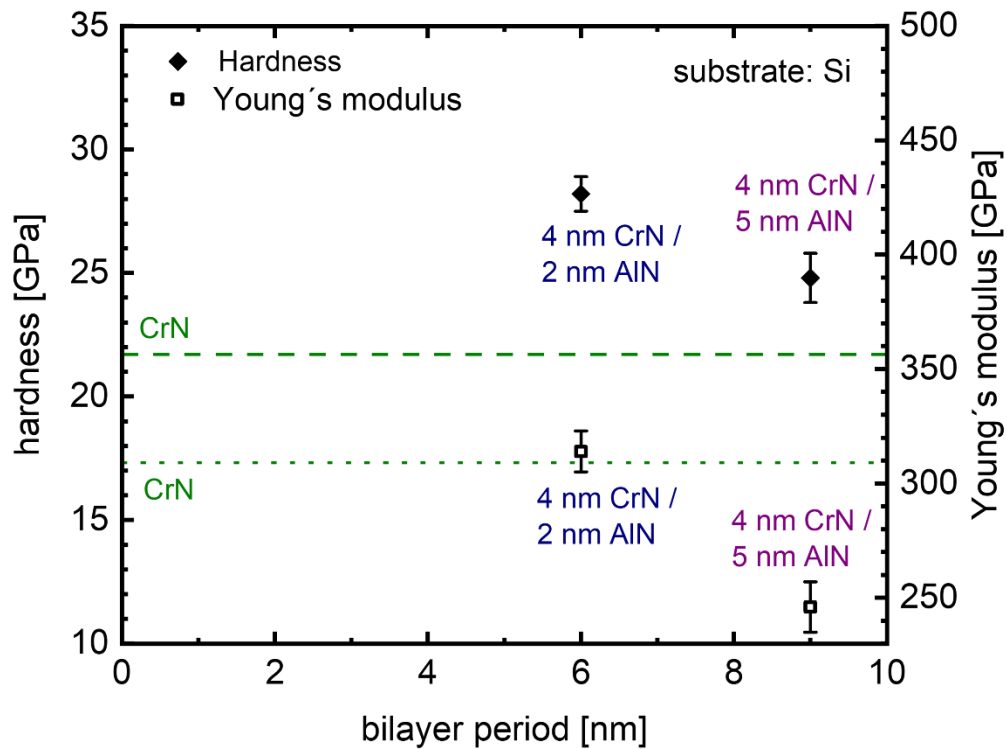


Figure 25: measured hardness and Young's modulus of films on Si (100) substrates.

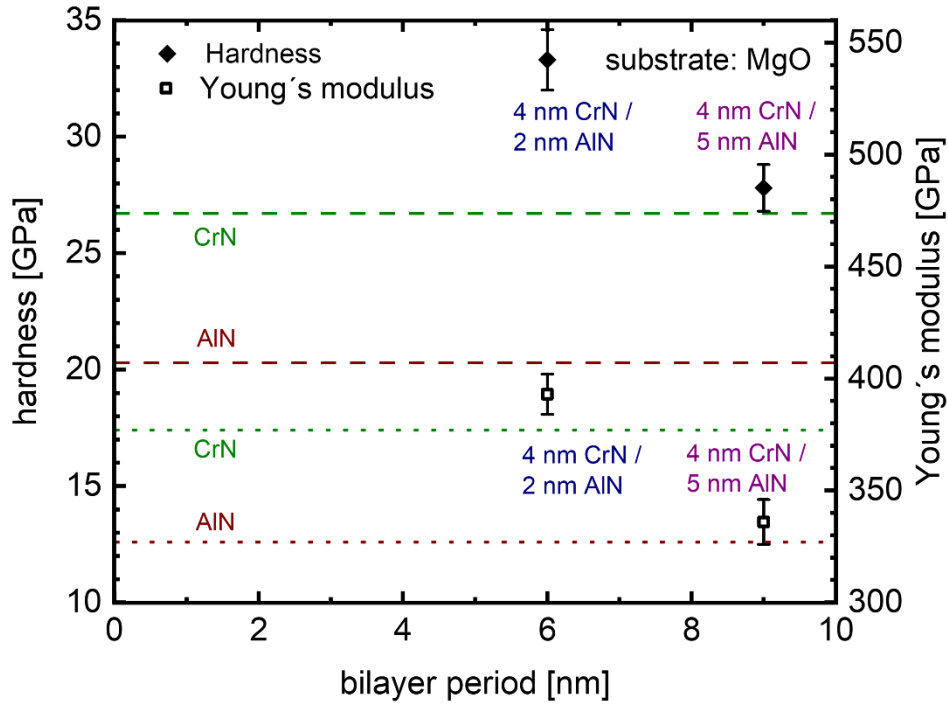


Figure 26: measured hardness and Young's modulus of films on MgO (100) substrates.

**Influence of the bilayer period on SL hardness**

The present set of films contains two different multilayer architectures, with the main difference being the AlN structure. The hardness enhancement of SL films is, also without a change in structure, strongly dependent on the bilayer period. As shown in Figure 27 and Figure 28, there is a peak in hardness at a certain bilayer period.

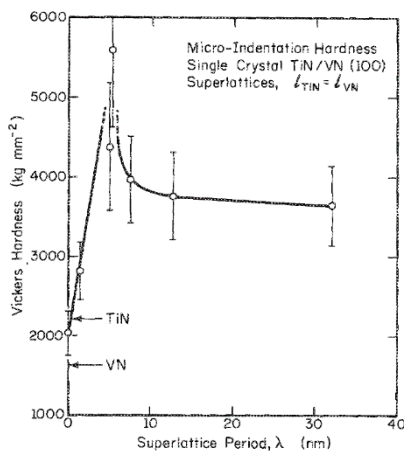


Figure 27: dependency of hardness on the bilayer period [59].

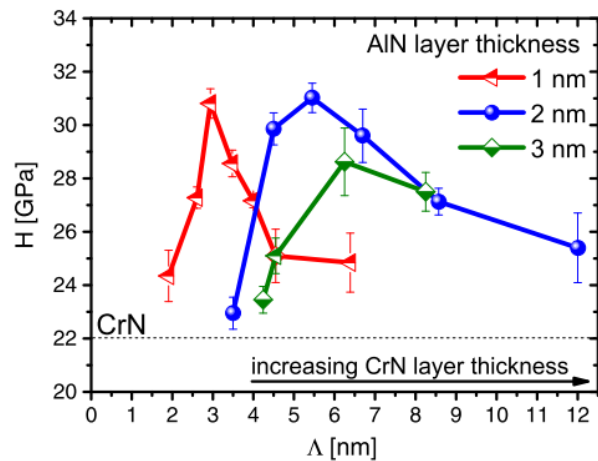


Figure 28: dependency of hardness on the bilayer period and individual layer thicknesses [48].

Chu and Barnett [54] proposed a model for the enhancement of hardness and yield strength in SL films with miscible materials and equal slip systems, which is based on the shear stress needed for dislocation movement. This shear stress is proportional to the yield stress, which can be related to the hardness with  $\sigma_y \sim H/3$ .

Two mechanisms are mainly responsible for the increase in required shear stress: Due to a difference in shear moduli, dislocation glide across the layer interface into the layer with the higher shear modulus is inhibited and due to the small layer thickness, dislocation glide within individual layers is inhibited. The dependency on bilayer period with a peak at a certain value can be attributed to their influences at different bilayer periods. More precisely, not only the bilayer period, but the entire composition modulation is important. It is described by the layer thicknesses of individual layers, the interface width, and the composition amplitude of the layers.

The decrease of required shear stress at small bilayer periods can be attributed to the dependence of the shear stress enhancement on the difference in shear moduli and the interface width. At, in relation to the interface width, sufficiently small layer thicknesses the composition amplitude and consequently also the difference in shear moduli decreases. This leads to a decrease of the shear stress and in hardness. Additionally, by increasing the interface width the maximum shear stress is also decreased.

At high bilayer periods, dislocation movement in the layers is possible more easily. Dislocation movement can occur in both layers. The needed shear stress for dislocation movement decreases with layer thickness, it is dependent on whether an existing dislocation is moved, or dislocations have to be generated and moved, and on the layer material. The yield stress for dislocation movement in both layer materials contributes proportioned to the total yield stress [54].



### Influence of substrate

Figure 29 and Figure 31 show the mechanical properties of single crystalline SL films on MgO (100) and polycrystalline SL films on Si (100) substrates. Higher hardness values and Young's moduli were observed for all architectures on MgO (100) substrates, compared with their polycrystalline counterparts.

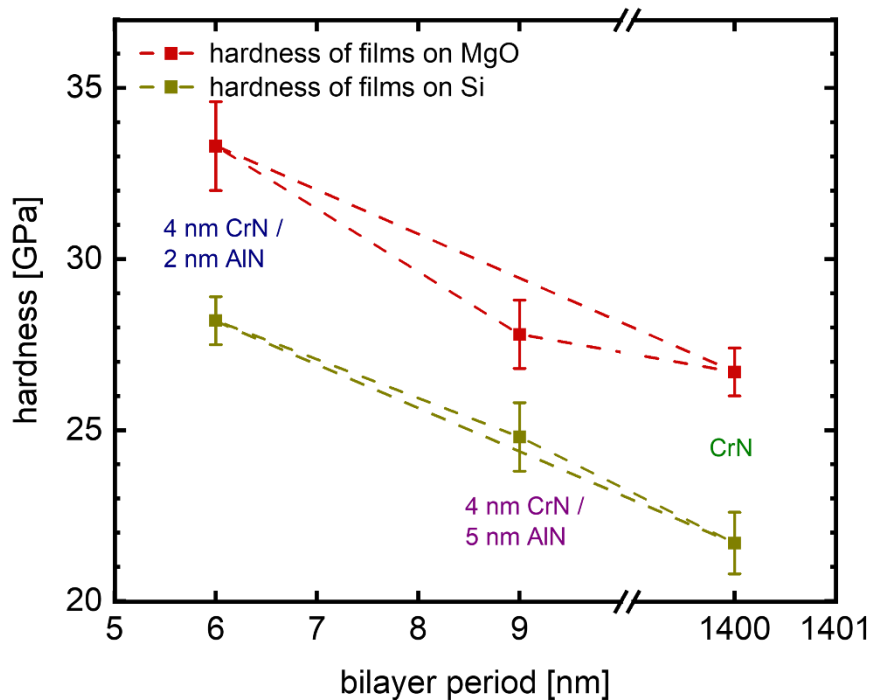


Figure 29: measured hardness of films on Si (100) and MgO (100).

Monolithic CrN films on MgO (100) substrate show a 5 GPa higher hardness than the same films on Si (100). Due to the presence/absence of grain boundaries, the plastic deformation behavior is different. While slip deformation occurs in single crystals, deformation of polycrystals is governed by grain boundary slip and grain rotation [55]. Another reason why higher hardness values are measured for films on MgO (100) substrates could be compressive residual stresses in the films. The latter arise when the film-substrate composite cools down from deposition temperature to room temperature due to the higher coefficient of thermal expansion of MgO compared to CrN and AlN. The thermal expansion coefficient of Si is lower compared to that of the film materials, resulting in the formation of tensile thermal stresses in the films. Compressive residual stresses (apparently) enhance the hardness of the films [2].

The hardness of SL films with 4 nm CrN / 2 nm AlN architecture is also approximately 5 GPa higher on MgO (100) substrates than on Si (100) substrates.

Chen et al. [50,56] lately investigated the difference in deformation and strengthening behavior of TiN/AlN SL films during nanoindentation with a cube corner tip and high loads. In polycrystalline SLs, grain boundary sliding was identified as the main deformation mechanism. In single crystalline SL films, in different regions different mechanisms, like interface distortion, SL slip deformation, and solid solution formation with polycrystalline grain rotation, were observed (Figure 30). Based on the observed difference in deformation behavior, a different strengthening behavior was suggested for single crystalline and polycrystalline SL films [56].

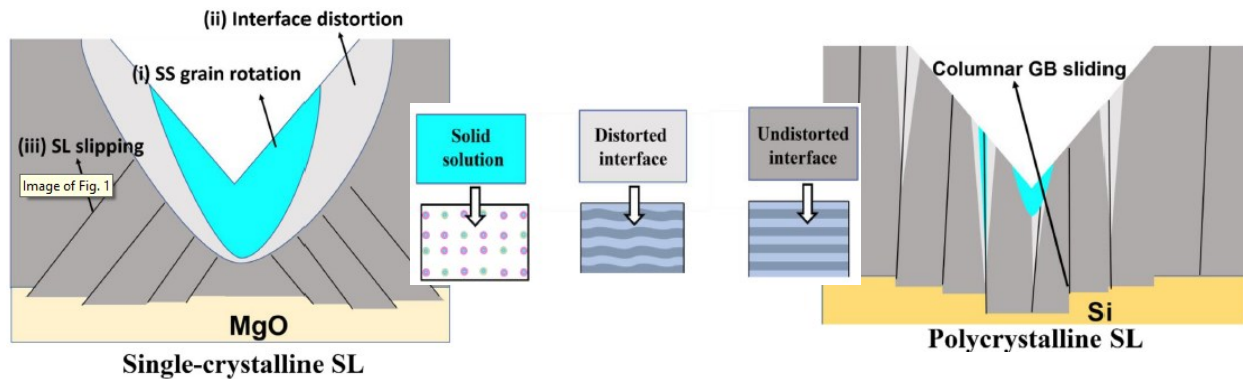


Figure 30: deformation zones and mechanisms in single crystalline and polycrystalline TiN/AlN SL films [56].

In the present work, it was found that the excess hardness of the SL films compared to monolithic CrN is approximately the same, regardless of the substrate type on which the films were grown. Specific deformation mechanisms and active strengthening mechanisms remain to be investigated.

A lower difference in hardness of approximately 3 GPa was observed in films with 4 nm CrN / 2 nm AlN architecture. On both substrates, the films were polycrystalline with a comparable crystallographic texture (Figure 21).

Figure 31 shows the difference in Young's moduli of films on different substrates. In all films on MgO (100), the measured Young's modulus is 70-90 GPa higher than in films on Si (100).

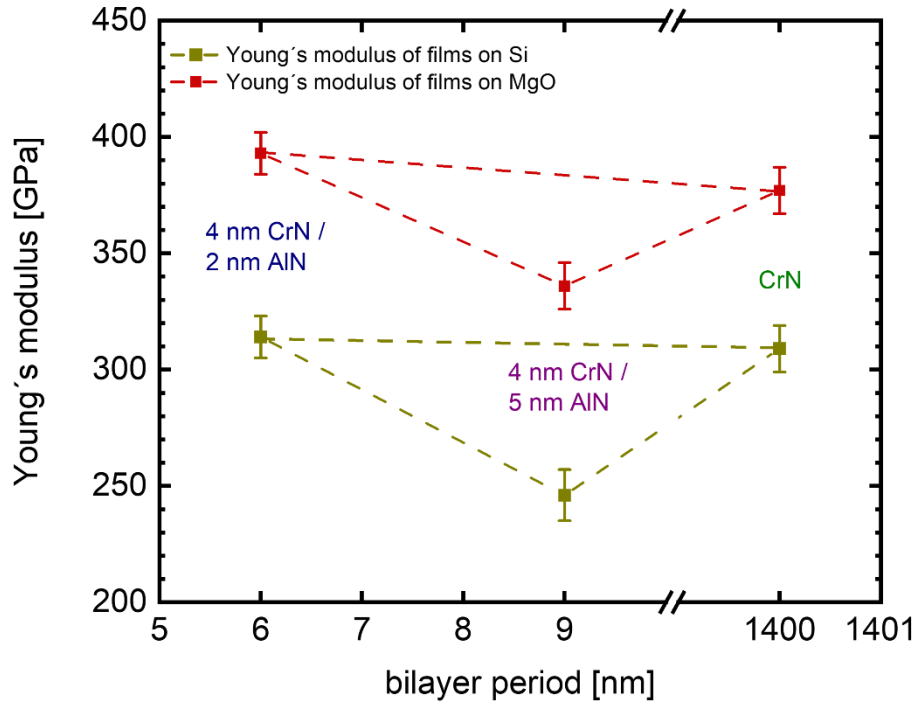


Figure 31: measured Young's moduli of films on Si (100) and MgO (100) substrates.

## 5. Summary

Within this work, CrN/AlN SL coatings were synthesized and characterized. The main goal was the deposition of SLs with fully stabilized B1-AlN structure. In addition, the corresponding monolithic films and a multilayer were produced in which the critical layer thickness of cubic AlN was exceeded and B3-AlN was thus formed. In addition, the influence of substrate on the film properties was investigated. The structural and mechanical properties of the above listed coatings were determined and compared.

Reactive magnetron sputtering was chosen as the film synthesis method. A comprehensive deposition parameter study was necessary for the choice of deposition parameters. A main result of the preliminary study was that reducing the total pressure to 2  $\mu\text{bar}$  leads to dense and hard coatings. Material-specific behavior of CrN and AlN and the need of keeping most deposition conditions constant over the whole deposition process required a trade-off in deposition parameter selection. Opposing requirements in terms of nitrogen consumption and the desired structural properties were compensated by adjusting the individual target powers.

The critical layer thickness for crack formation in monolithic CrN films was determined experimentally to be in the range of 1.40–1.47  $\mu\text{m}$ , which matched well with theoretical predictions based on the concept of energy release rate and linear elastic fracture mechanics.

Deposition of SL architectures was realized by computer-controlled shutters which opened and closed alternately. Processes were optimized as far as possible. In the end, 4 nm CrN / 2 nm AlN SL films, 4 nm CrN / 5 nm AlN multilayer films, as well as monolithic CrN and AlN films were deposited. Polycrystalline films were deposited on Si (100) substrates, while during the same deposition run, single-crystalline films were grown on MgO (100) substrates. Additionally, austenitic steel substrates were coated.

Film characterization focused on structural and mechanical properties of the films on Si (100) and MgO (100) substrates. X-ray diffraction was used for structure analysis, laser confocal microscopy to measure the total film thickness and nanoindentation measurements gave the hardness and Young's modulus of the films.

X-ray diffraction revealed the single crystalline and polycrystalline character of films on MgO (100) and Si (100) substrates, respectively. Also preferred growth orientations were determined and with satellite peak positions the bilayer periods were calculated.

Results from film thickness measurements and nanoindentation experiments are summarized in Table 5:

*Table 5: Film thickness  $d$ , hardness  $H$  and Young's modulus  $E$  of different single crystalline and polycrystalline films.*

	Substrate = Si (100)			Substrate = MgO (100)		
	$d$ [ $\mu\text{m}$ ]	$H$ [GPa]	$E$ [GPa]	$d$ [ $\mu\text{m}$ ]	$H$ [GPa]	$E$ [GPa]
CrN	1.38	21.7 $\pm$ 0.9	309 $\pm$ 10	1.30	26.7 $\pm$ 0.7	377 $\pm$ 10
CrN/AlN 4/2	1.67	28.2 $\pm$ 0.7	314 $\pm$ 9	1.45	33.3 $\pm$ 1.3	393 $\pm$ 9
CrN/AlN 4/5	0.71	24.8 $\pm$ 1.0	246 $\pm$ 11	0.69	27.8 $\pm$ 1.0	336 $\pm$ 10

The highest hardness and Young's moduli were obtained in 4 nm CrN / 2 nm AlN films with fully stabilized B1-AlN. Compared to monolithic CrN an increase in hardness of 6.5 GPa was observed on both substrates. Two different mechanisms are responsible for the bilayer period dependent increase in hardness. Due to the small layer thicknesses, dislocation glide within layers is inhibited and due to the difference in shear moduli dislocation movement across the interfaces is inhibited. As a result of the higher bilayer period and the appearance of B3 AlN, the hardness in 4 nm CrN / 5 nm AlN films was significantly lower than in 4 nm CrN / 2 nm AlN films. Comparing single crystalline and polycrystalline films, hardness was 5 GPa higher in single crystalline CrN and 4 nm CrN / 2 nm AlN films deposited on MgO (100) substrates.

With the synthesis of films for this thesis, SL film deposition was realized with the used deposition system for the first time. Thereby the preconditions for depositing various other SLs with this device were created.

## 6. References

- [1] C. Mitterer, in V. Sarin (ed.), D. Mari (ed.), L. Llanes (ed.), C. Nebel (ed.), “Comprehensive hard materials,” Elsevier, 2014, 449–467.
- [2] P.H. Mayrhofer, C. Mitterer, L. Hultman, H. Clemens, Microstructural design of hard coatings, *Progress in Materials Science* 51 (2006) 1032–1114.
- [3] N. Schalk, M. Tkadletz, C. Mitterer, Hard coatings for cutting applications: Physical vs. chemical vapor deposition and future challenges for the coatings community, *Surface and Coatings Technology* 429 (2022) 127949.
- [4] A. Inspektor, P.A. Salvador, Architecture of PVD coatings for metalcutting applications: A review, *Surface and Coatings Technology* 257 (2014) 138–153.
- [5] S.A. Barnett, in M. Francombe (ed.), J. Vossen (ed.), “Physics of Thin Films: Mechanic and dielectric properties,” Academic Press, San Diego, 1993, 1–77.
- [6] R. Mundotia, T. Ghorude, D.C. Kothari, A. Kale, N. Thorat, Tuning bilayer period of AlN/CrN superlattice coatings deposited using cathodic arc technique for superior mechanical properties and thermal stability, *Applied Surface Science Advances* 7 (2022) 100205.
- [7] L. Hultman, in A. Cavaleiro (ed.), J. de Hosson (ed.), “Nanostructured coatings,” Springer Science + Business Media, New York, 2007, 539–554.
- [8] B.M. Clemens, H. Kung, S.A. Barnett, Structure and strength of multilayers, *MRS Bulletin* 24 (1999) 2026.
- [9] R.F. Zhang, S. Veprek, Deformation paths and atomistic mechanism of B4 → B1 phase transformation in aluminium nitride, *Acta Materialia* 57 (2009) 2259–2265.
- [10] R.F. Zhang, S.H. Sheng, S. Veprek, Mechanism of the B3 to B1 transformation in cubic AlN under uniaxial stress, *Physical Review B - Condensed Matter and Materials Physics* 76 (2007) 1–5.
- [11] H. Xiang, H. Li, T. Fu, Y. Zhao, C. Huang, G. Zhang, X. Peng, Molecular dynamics simulation of AlN thin films under nanoindentation, *Ceramics International* 43 (2017) 4068–4075.

- [12] W. Lengauer, P. Ettmayer, "Ullmann's Encyclopedia of industrial Chemistry," Verlag Chemie, Weinheim, 2012, 227–249.
- [13] V. Antonov, I. Iordanova, "First principles study of crystallographic structure and elastic properties of chromium nitride," AIP Conference Proceedings 1203 (2010) 1149–1154.
- [14] P. Franke, D. Neuschütz, "Thermodynamic Properties of Inorganic Materials: Binary systems Part 2: Elements and Binary Systems from B - C to Cr - Zr," Springer Nature Switzerland AG, 2004, 84.
- [15] H. Era, Y. Ide, A. Nino, K. Kishitake, TEM study on chromium nitride coatings deposited by reactive sputter method, Surface and Coatings Technology 194 (2005) 265–270.
- [16] H.A. Wriedt, in T. Massalski (ed.), J. Murray (ed.), H. Baker (ed.), "Binary alloy phase diagrams: Volume 1," William W. Scott, Jr, Ohio, 1986, 135–136.
- [17] V.S. Kudyakova, R.A. Shishkin, A.A. Elagin, M. v. Baranov, A.R. Beketov, Aluminium nitride cubic modifications synthesis methods and its features. Review, Journal of the European Ceramic Society 37 (2017) 1143–1156.
- [18] M. Schlögl, C. Kirchlechner, J. Paulitsch, J. Keckes, P.H. Mayrhofer, Effects of structure and interfaces on fracture toughness of CrN/AlN multilayer coatings, Scripta Materialia 68 (2013) 917–920.
- [19] M. Bartosik, M. Todt, D. Holec, J. Todt, L. Zhou, H. Riedl, H.J. Böhm, F.G. Rammerstorfer, P.H. Mayrhofer, Thermal expansion of rock-salt cubic AlN, Applied Physics Letters 107 (2015) 071602.
- [20] D. Chen, X.L. Ma, Y.M. Wang, Thickness-dependent structural transformation in the AlN film, Acta Materialia 53 (2005) 5223–5227.
- [21] Z. Chen, D. Holec, M. Bartosik, P.H. Mayrhofer, Z. Zhang, Crystallographic orientation dependent maximum layer thickness of cubic AlN in CrN/AlN multilayers, Acta Materialia 168 (2019) 190–202.
- [22] M. Ohring, "Materials Science of Thin Films: Deposition & Structure," Academic Press, 2002, 95–96, 145–147, 211–222.

- [23] P.M. Martin, "Deposition technologies for films and coatings," Elsevier Inc, Oxford, 2005, 9–141.
- [24] J.T. Gudmundsson, D. Lundin, in J.T. Gudmundsson (ed.), D. Lundin (ed.), T. Minea (ed.), "High Power Impulse Magnetron Sputtering," Elsevier, Amsterdam, Oxford, Cambridge, 2020, 1–48.
- [25] R. Dedoncker, The Role of Reactive Gases during Sputter Deposition of Complex Alloys, PhD thesis, Universitaet Gent, 2021.
- [26] W. Kern, K. Schuegraf, in K. Seshan (ed.), "Handbook of thin-film deposition: Processes and Technologies," Noyes Publications/William Andrew Pub, Norwich, 2002, 11–44.
- [27] K. Sarakinos, L. Martinu, in J.T. Gudmundsson (ed.), D. Lundin (ed.), T. Minea (ed.), "High Power Impulse Magnetron Sputtering," Elsevier, 2020, 333–374.
- [28] R. Daniel, J. Musil, "Novel Nanocomposite Coatings: Advances and Industrial Applications," Pan Stanford Publishing, Boca Raton, Florida, 2013, 27–86.
- [29] P.B. Barna, M. Adamik, Fundamental structure forming phenomena of polycrystalline films and the structure zone models, *Thin Solid Films* 317 (1998) 27–33.
- [30] J.A. Thornton, Influence of apparatus geometry and deposition conditions on the structure and topography of thick sputtered coatings, *Thin Solid Films* 666 (2014) 2–7.
- [31] A. Anders, A structure zone diagram including plasma-based deposition and ion etching, *Thin Solid Films* 518 (2010) 4087–4090.
- [32] R. Daniel, M. Meindlhumer, W. Baumegger, J. Zalesak, B. Sartory, M. Burghammer, C. Mitterer, J. Keckes, Grain boundary design of thin films: Using tilted brittle interfaces for multiple crack deflection toughening, *Acta Materialia* 122 (2017) 130–137.
- [33] J.B. Wachtman, W.R. Cannon, M.J. Matthewson, "Mechanical Properties of Ceramics," John Wiley & Sons, Hoboken, NJ, USA, 2009, 27–34.
- [34] T.H. Courtney, "Mechanical Behavior of Materials," Waveland Press, Long Grove, Illinois, 2009, 175–210.
- [35] S. Barnett, A. Madan, Superhard superlattices, *Physics World* 11 (1998) 45–48.



- [36] Bruker, Web page, <https://www.bruker.com/en/products-and-solutions/diffractometers-and-scattering-systems/x-ray-diffractometers/diffrac-suite-software/diffrac-topas.html>, September 2022.
- [37] K. Bobzin, T. Brögelmann, R.H. Brugnara, M. Arghavani, T.S. Yang, Y.Y. Chang, S.Y. Chang, Investigation on plastic behavior of HPPMS CrN, AlN and CrN/AlN-multilayer coatings using finite element simulation and nanoindentation, *Surface and Coatings Technology* 284 (2015) 310–317.
- [38] W.C. Oliver, G.M. Pharr, An improved technique for determining hardness and elastic modulus using load and displacement sensing indentation experiments, *Journal of Materials Research* 7 (1992) 1564–1583.
- [39] X. Gu, Z. Zhang, M. Bartosik, P.H. Mayrhofer, H. Duan, Dislocation densities and alternating strain fields in CrN/AlN nanolayers, *Thin Solid Films* 638 (2017) 189–200.
- [40] M. Bartosik, J. Keckes, P.O.Å. Persson, H. Riedl, P.H. Mayrhofer, Interface controlled microstructure evolution in nanolayered thin films, *Scripta Materialia* 123 (2016) 13–16.
- [41] J. Todt, C. Krywka, Z.L. Zhang, P.H. Mayrhofer, J. Keckes, M. Bartosik, Indentation response of a superlattice thin film revealed by in-situ scanning X-ray nanodiffraction, *Acta Materialia* 195 (2020) 425–432.
- [42] L.B. Freund, S. Suresh, “Thin Film Materials - Stress, Defect formation and Surface Evolution,” Cambridge University Press, Cambridge, 2003, 309–324.
- [43] J.W. Hutchinson, Z. Suo, in J. Hutchinson (ed.), T. Wu (ed.), “Advances in Applied Mechanics,” Academic Press, San Diego, London, 1992, 126–146.
- [44] P.H. Mayrhofer, G. Tischler, C. Mitterer, Microstructure and mechanical/thermal properties of Cr-N coatings deposited by reactive unbalanced magnetron sputtering, *Surface and Coatings Technology* 142–144 (2001) 78–84.
- [45] H. Haftbaradaran, X. Xiao, H. Gao, Critical film thickness for fracture in thin-film electrodes on substrates in the presence of interfacial sliding, *Modelling and Simulation in Materials Science and Engineering* 21 (2013) 074008.

- [46] A. Favache, L. Libralesso, P.J. Jacques, J.P. Raskin, C. Bailly, B. Nysten, T. Pardoën, Fracture toughness measurement of ultra-thin hard films deposited on a polymer interlayer, *Thin Solid Films* 550 (2014) 464–471.
- [47] J.L. Beuth, Cracking of thin bonded films in residual tension, *International Journal of Solids and Structures* 29 (1992) 1657–1675.
- [48] M. Schlögl, B. Mayer, J. Paulitsch, P.H. Mayrhofer, Influence of CrN and AlN layer thicknesses on structure and mechanical properties of CrN/AlN superlattices, *Thin Solid Films* 545 (2013) 375–379.
- [49] J. Pellegrino, S.B. Qadri, P.M. Amirtharaj, N. v. Nguyen, J. Comas, Interface sharpness in low-order III-V superlattices, *Thin Solid Films* 220 (1992) 176–183.
- [50] Z. Chen, Y. Zheng, Y. Huang, Z. Gao, H. Sheng, M. Bartosik, P.H. Mayrhofer, Z. Zhang, Atomic-scale understanding of the structural evolution of TiN/AlN superlattice during nanoindentation— Part 1: Deformation, *Acta Materialia* 234 (2022) 118008.
- [51] X. Chu, M.S. Wong, W.D. Sproul, S.L. Rohde, S.A. Barnett, Deposition and properties of polycrystalline TiN/NbN superlattice coatings, *Journal of Vacuum Science & Technology A* 10 (1992) 1604–1609.
- [52] M. Shinn, L. Hultman, S.A. Barnett, Growth, structure, and microhardness of epitaxial TiN/NbN superlattices, *Journal of Materials Research* 7 (1992) 901–911.
- [53] J. Lin, J.J. Moore, B. Mishra, M. Pinkas, W.D. Sproul, Nano-structured CrN/AlN multilayer coatings synthesized by pulsed closed field unbalanced magnetron sputtering, *Surface and Coatings Technology* 204 (2009) 936–940.
- [54] X. Chu, S.A. Barnett, Model of superlattice yield stress and hardness enhancements, *Journal of Applied Physics* 77 (1995) 4403–4411.
- [55] G. Yang, S.J. Park, Deformation of single crystals, polycrystalline materials, and thin films: A review, *Materials* 12 (2019) 2003.

- [56] Z. Chen, Y. Zheng, Y. Huang, Z. Gao, H. Sheng, M. Bartosik, P.H. Mayrhofer, Z. Zhang, Atomic-scale understanding of the structural evolution in TiN/AlN superlattice during nanoindentation—Part 2: Strengthening, *Acta Materialia* 234 (2022) 118009.
- [57] N. Koutná, P. Řehák, Z. Chen, M. Bartosik, M. Fallmann, M. Černý, Z. Zhang, M. Friák, M. Šob, P.H. Mayrhofer, D. Holec, Correlating structural and mechanical properties of AlN/TiN superlattice films, *Scripta Materialia* 165 (2019) 159–163.
- [58] T. Wonglakhon, D. Zahn, Interaction potentials for modelling GaN precipitation and solid state polymorphism, *Journal of Physics Condensed Matter* 32 (2020) 205401.
- [59] U. Helmersson, S. Todorova, S.A. Barnett, J.E. Sundgren, L.C. Markert, J.E. Greene, Growth of single-crystal TiN/VN strained-layer superlattices with extremely high mechanical hardness, *Journal of Applied Physics* 62 (1987) 481–484.